18th AIAA/CEAS Aeroacoustics Conference (33rd AIAA Aeroacoustics Conference)
04 - 06 June 2012, Colorado Springs, CO

AIAA 2012-2214

Axisymmetry and azimuthal modes in jet noise

Håvard Vold* and Parthiv Shah†
ATA Engineering, Inc., San Diego, CA, 92130

Philip Morris‡ and Yongle Du§
Pennsylvania State University, University Park, PA, 16802

Dimitri Papamoschou¶
University of California, Irvine, Irvine, CA, 92697-3975

This paper will show that the matrix of all noise spectra radiated from a jet in a stationary condition, axisymmetric in construction and boundary conditions, has a special invariant structure which simplifies measurements and enables the total composite noise field to be expressed as a sum of mutually incoherent partial fields. Each such partial field is described in terms of an azimuthal mode with a integer wave number and polarity. The consequences of this structure include a simple explanation of the nature of azimuthal coherence and a practical procedure for estimating the dominant partial fields of the jet from measurements with a limited azimuthal coverage. It should be noted that the conclusions are only drawn from the assumptions of stationarity and axisymmetry, such that both large and fine scale mixing noise and broadband shock associated noise are covered by this theory. This paper also introduces a concept of *sound flares* as a model for how random fluid dynamic events in a turbulent flow superpose stochastically to produce measured spectra and crossspectra in the linear hydrodynamic and acoustic fields. This concept may be applied to model both axisymmetric as well as noncircular nozzles.

Nomenclature

$\bar{G}_{PP}$ Improved spectral estimator
$\Gamma(\{\phi_1, r_1, x_1\}, \{\phi_2, r_2, x_2\})$ General crossspectral function
$\gamma^2(\phi_1, \phi_2)$ Coherence between angles ϕ_1 and ϕ_2
$\mathcal{A}_m(r)$ Azimuthal mode coefficient
$\mathcal{P}$ Helical spectrum
$\mathcal{Z}$ The set of integers
ω Generic frequency variable
ϕ Azimuthal coordinate
ρ_m Amplitude of partial field m from eigenanalysis of autospectral matrix
$\tilde{G}_{PP}$ Generic spectral estimator

*Corresponding Author, Vice President and Senior Technical Fellow, AIAA Associate Fellow; hvold@ata-e.com
†Senior Project Engineer, AIAA Senior Member
‡Boeing/A. D. Welliver Professor of Aerospace Engineering, AIAA Fellow
§Postdoctoral Fellow, Department of Aerospace Engineering, AIAA Student Member
¶Professor of Aerospace Engineering, AIAA Fellow

$\tilde{p}(t)$ Complex vector time history of pressures in azimuthal coordinates
$\tilde{p}_m(t)$ Complex scalar time history of azimuthal wave number m
D Diameter of jet nozzle
$E()$ The expectation operator
$g_n(r_1, x_1, r_2, x_2)$ Fourier coefficient of axisymmetric crossspectral function
$g_{nm}(r_1, x_1, r_2, x_2)$ Fourier coefficient of general crossspectral function
G_{PP} Autospectral matrix of pressure measurements
$H_n^{(1)}(r)$ Hankel function of the first kind[1]
$h_n^{(1)}(r)$ Spherical Hankel function of the first kind[1]
$h_A(\phi)$ Azimuthal probability density function
$h_X(\phi)$ Axial probability density function
k Acoustic wavenumber
k_c Convective wavenumber
k_r Radial wavenumber
k_x Axial wavenumber
L Axial extent of wave packet
N Number of microphones in ring
$p(\phi, r, x)$ Random pressure function at location (ϕ, r, x)
$P(t)$ Vector time history of pressures at the microphone locations
$P_n(r, x)$ Random pressure function associated with azimuthal mode n
$P_n^m(\cos\theta)$ Associated Legendre function[1]
Q Simple permutation matrix
R Radius of measurement circle
r Radial coordinate
V_m Partial field corresponding to the amplitude ρ_m
W Matrix of azimuthal mode shapes
W_m Azimuthal mode shape of wave number m
x Axial distance along jet centerline
LES Large Eddy Simulations
NAH Nearfield Acoustic Holography
POD Proper Orthogonal Decomposition, also known as *partial field decomposition*

I. Introduction

The two major sources of jet engine exhaust noise are turbulent mixing noise and shock-associated noise. In addition, internal engine noise is likely to radiate, but at a lower level. The dominant turbulent mixing noise is generated by large-scale turbulent structures. For high-speed jets typical of military engines, these structures convect supersonically with respect to the ambient speed of sound, and generate highly directed *Mach wave* or *instability wave* radiation in the downstream direction. The actual peak noise angle is determined by the convection velocity of the turbulence. *Broadband shock-associated noise* (BBSAN) is generated by the interaction between the turbulence in the jet shear layer and the jets shock cell structure. Because of the simple geometric design of military aircraft engine exhaust nozzles, shock cells are always present in the jet plume. Broadband shock-associated noise dominates the noise radiation in the forward arc.

Large turbulence structures in jets are a form of Kelvin-Helmholtz shear layer instability that arise in the presence of a mean-velocity profile that is inflectional.[2] The connection between the radiated noise of high-speed jets and this instability has been described by a number of authors ([3,4,5]). The stochastic instability wave model is in essence statistically equivalent to the large tur-

bulence structures in the jet, and may be described approximately by the physics of a supersonically convecting wavy wall with the same wavelength and wave speed.[6] This model accurately predicts the direction of the most intense noise radiation, and the *Strouhal number* of the most amplified instability wave is found to match the Strouhal number at the peak of the radiated noise spectrum. Stochastic noise propagation models must account for the rapid growth and more gradual decay of the amplitude of the wavy wall-like instability waves. Such amplitude-modulated wavepackets have been described mathematically by numerous works ([7,8,9,10]). The wavepacket function has been used successfully to parameterize the source of high-speed jets and the resulting source model has been used for computing the scattering of sound from those jets around aircraft surfaces using the boundary element method.[11] An alternative approach to the modeling of wavepackets is to perform the eigen-decomposition of the auto-spectral matrix and present the weighted eigenvectors as *partial fields*, or principal components. Partial fields may be used directly as quantitative expressions of the traveling wavepackets or may be used to fit physics-based reduced order models.[12,13,14]

Organized turbulence structures have been detected at model-scale by a number of researchers ([15,16,17]) using near-field measurement arrays in the linear hydrodynamic regime. The detection technique involves fitting the eigenfunctions of the instability wave model to measured data in the jet near-field. An essential requirement of the data is knowledge of the space-time correlation in time domain, or, equivalently, the cross-spectral matrix in frequency domain. Without an optimization strategy, a full mapping of the auto-spectral matrix of a large number of sensor locations would require an enormous number of microphones or extremely long acquisition times. This paper is motivated by the practical need of an efficient process to map out the essential cross-spectral information that allows physical modeling of the noise source. At the same time, the methods developed help our understanding of the fundamental physics of jet noise generation. The emphasis here is on axisymmetric jets; however, it will be shown the tools developed are generic enough to be applied to non-symmmetric jets.

In this paper we introduce the mathematics of azimuthal symmetry, and from there present the applications. Measurements of jet noise using microphone arrays have been used in recent years to attempt to understand the characteristics of the sources of jet noise. These measurements have been made in both the near and far acoustic fields of the jet. Processing of the measured data can involve traditional *beamforming*, often coupled with a *deconvolution* algorithm, and *Nearfield Acoustic Holography*. In the latter case the data can be projected to the the far field. Projection to the far field can also be achieved by using the measured near field pressures coupled with a tailored *Green's function* based on the shape of the array.

A question that often arises in the design of the array is its azimuthal coverage. From a practical point of view there is an advantage of limiting the coverage. Clearly, for a fixed number of microphones, the resolution will be improved as the azimuthal coverage is reduced. There are also situations where a full 360° coverage would be extremely difficult. In the case of a full scale engine, for example, it would be challenging, but not impossible, to have a near field array which encloses the jet plume. It would be very helpful if the array only needed to cover a limited azimuthal extent. However, can the azimuthal modal content of the near field pressure be determined? That is the subject of the present paper.

- At most 180 degrees need be measured, a smaller sector will suffice when the required number of azimuthal modes is low. Section II.B.
- The POD (eigenvectors, singular vectors, partial fields) structure of the spectral matrix shows a complete algebraic and stochastic decoupling between the different possible azimuthal wave numbers. Sections II.A.2 and III.A.
  - The decoupling also allows for a definition of azimuthal wave packets that constitute a

complete basis for the total noise sound field.

- Loss of azimuthal coherence must be due to the interaction of at least two strong azimuthal modes. Section II.C.
- Smaller angular coverage allows a higher spatial density of instrumentation for the capture of higher wave numbers.
- The angular origin invariance permits a more statistically efficient estimation of autospectra and crossspectra. Sections II.D and III.C

Organization of the paper

We will start the theoretical exposition of spectral function properties with a continuum section that derives results which do not presuppose a grid of measurement locations, section II, followed by a section that assumes a finite grid of measurements, section III. Next, we have a section on a *sound flare* random pressure event noise model, section IV, and finally examples from the theoretical developments applied to data from model scale tests and LES experiments, section V.

II. Continuum analysis

This paper will specialize to the stationary behavior of a jet at a generic frequency ω, which will be dropped from the notation without any loss of understanding.

We shall consider an axisymmetric jet under stationary operation, with measurements taken on a surface of revolution aligned with and centered on the axis of the jet. We shall use a cylindrical coordinate system, $\{\phi, r, x\}$, where ϕ is the azimuthal angle, r is the radial distance from the centerline, and x is the axial distance along the centerline. The origin is taken at the jet exit, even though this is arbitrary. The pressure perturbation $p(\phi, r, x)$ measured at any point is a random function of the spatial coordinates.

We shall restrict our measurements to the region of space where the pressure field satisfies the *Helmholtz* equation, such that we exclude any nonlinearities, but include the linear part of the hydrodynamic field.

II.A. The crossspectral function

This section first derives some basic properties for the crossspectral function for all jets, and then adds the constraint of axisymmetry.

II.A.1. The general crossspectral function of the pressure for arbitrary jets

We define the *general crossspectral* function between two points $\{\phi_1, r_1, x_1\}$ and $\{\phi_2, r_2, x_2\}$ as

$$\Gamma(\{\phi_1, r_1, x_1\}, \{\phi_2, r_2, x_2\}) = E(p(\phi_1, r_1, x_1)\overline{p(\phi_2, r_2, x_2)}), \tag{1}$$

where E is the *expectation* or averaging operator, and the overline denotes complex conjugation. It also follows from equation (1) that

$$\overline{\Gamma(\{\phi_1, r_1, x_1\}, \{\phi_2, r_2, x_2\})} = \Gamma(\{\phi_2, r_2, x_2\}, \{\phi_1, r_1, x_1\}). \tag{2}$$

Because of the nature of cylindrical coordinates, the crossspectral function is also periodic in the two azimuthal coordinates, i.e.,

$$\Gamma(\{\phi_1 + 2m\pi, r_1, x_1\}, \{\phi_2 + 2n\pi, r_2, x_2\}) = \Gamma(\{\phi_1, r_1, x_1\}, \{\phi_2, r_2, x_2\}), \text{ for } m, n \in \mathcal{Z}. \tag{3}$$

II.A.2. The crossspectral function for axisymmetric jets

We now specialize to an axisymmetric jet, and note that the origin of the azimuthal coordinate ϕ is arbitrary. It follows that for any arbitrary angle ϕ_o, the crossspectral function must be invariant under the transformation $\phi \Rightarrow \phi + \phi_o$, i.e.,

$$\Gamma(\{\phi_1 + \phi_o, r_1, x_1\}, \{\phi_2 + \phi_o, r_2, x_2\}) = \Gamma(\{\phi_1, r_1, x_1\}, \{\phi_2, r_2, x_2\}). \tag{4}$$

By choosing $\phi_o = -\phi_1$, equation (4) reduces to

$$\Gamma(\{\phi_1, r_1, x_1\}, \{\phi_2, r_2, x_2\}) = \Gamma(\{0, r_1, x_1\}, \{\phi_2 - \phi_1, r_2, x_2\}). \tag{5}$$

Now, since the crossspectral function is periodic in the azimuthal coordinates, it follows that there exists a Fourier series expansion in the second azimuthal argument, written as

$$\Gamma(\{\phi_1, r_1, x_1\}, \{\phi_2, r_2, x_2\}) = \sum_{n=-\infty}^{\infty} g_n(r_1, x_1, r_2, x_2) \exp 2\pi i n(\phi_2 - \phi_1), \tag{6}$$

where $g_n(r_1, x_1, r_2, x_2)$ is a deterministic function.

Now we look at the random function $p(\phi, r, x)$ and note that it is also periodic in the azimuthal argument, $p(\phi + 2\pi, r, x) = p(\phi, r, x)$. It hence has a Fourier series expansion

$$p(\phi, r, x) = \sum_{n=-\infty}^{\infty} P_n(r, x) \exp 2\pi i n\phi, \tag{7}$$

with $P_n(r, x)$ being a random function. We insert this Fourier series into the definition of the crossspectral function, equation (1) and obtain

$$\Gamma(\{\phi_1, r_1, x_1\}, \{\phi_2, r_2, x_2\}) = \sum_{n=-\infty}^{\infty} \sum_{m=-\infty}^{\infty} g_{nm}(r_1, x_1, r_2, x_2) \exp 2\pi i(n\phi_2 - m\phi_1), \tag{8}$$

where $g_{nm}(r_1, x_1, r_2, x_2) = E(P_m(r_1, x_1)\overline{P_n(r_2, x_2)})$. Comparing equations (6) and (8) for the axisymmetric case, we can conclude that

$$g_{nm}(r_1, x_1, r_2, x_2) = E(P_m(r_1, x_1)\overline{P_n(r_2, x_2)}) = 0 \text{ for all } m \neq n, \tag{9}$$

which implies that the random fields $P_n(r, x) \exp 2\pi i n\phi$ are mutually stochastically incoherent.

We have thus shown that the random noise field generated by an axisymmetric jet can be written as a sum of mutually incoherent sound fields that are pure azimuthal modes in the azimuthal coordinate, see equation (7). Note also that the azimuthal modes, with exception of mode zero, have polarities, such that the azimuthal modes of positive polarities describe modes traveling in one direction, the negative modes in the opposite direction. Furthermore, a slight rewrite of equation (6)

$$\Gamma(\{\phi_1, r_1, x_1\}, \{\phi_2, r_2, x_2\}) = \sum_{n=-\infty}^{\infty} \exp(-2\pi i n\phi_1) g_n(r_1, x_1, r_2, x_2) \exp 2\pi i n\phi_2, \tag{10}$$

shows that the partial field decomposition of the total sound field may be written as the sum of the products of the azimuthal function $\exp(2\pi i n\phi)$ with the eigenfunctions of the *positive semidefinite operator* $g_n(r_1, x_1, r_2, x_2)$. When our data are measured with at finite set of transducers locations, this operator g_n reduces to a *positive semidefinite hermitian* matrix.

II.B. Recovery of the complete spectral function from measurements over a smaller azimuthal sector

We shall furthermore specialize to two identical arrays of microphones located at azimuthal angles ϕ_1 and ϕ_2 , such that the two will coincide when $\phi_1 = \phi_2$ .We can then write equation (6) as

$$\Gamma(\phi_2 - \phi_1, \{r\}, \{x\}) = \sum_{n=-\infty}^{\infty} g_n(\{r\}, \{x\}) \exp 2\pi i n(\phi_2 - \phi_1), \tag{11}$$

since the radial and axial distances stay the same. This equation says that if we have measured $\Gamma(\phi, \{r\}, \{x\})$ in the interval $[0, \Phi]$, we immediately know this function also for $\phi \in [-\Phi, 0]$. Specifically, if $\Phi \geq \pi$ then the crossspectral function is known for the complete azimuthal span.

When the sector of measurements is smaller than π, we can still recover the entire spectral spectral function, but as we shall see, subject to possible numerical ill conditioning. To this end, multiply equation (11) by $\exp(im\phi)$ and integrate

$$\int_{-\Phi}^{\Phi} \exp(im\phi)\Gamma(\phi, \{r\}, \{x\})d\phi = \sum_{n=-N}^{N} g_n(\{r\}, \{x\}) \int_{-\Phi}^{\Phi} \exp\left(i(n-m)\phi\right)d\phi, \tag{12}$$

where we have limited the summation to a finite sum of dominant azimuthal modes. The integral on the right side of equation (12) has an analytical solution, transforming this equation to the form

$$\int_{-\Phi}^{\Phi} \exp(im\phi)\Gamma(\phi, \{r\}, \{x\})d\phi = \sum_{n=-N}^{N} g_n(\{r\}, \{x\}) 2\Phi \operatorname{sinc}((m-n)\Phi), \tag{13}$$

with $sinc(x) = \sin(x)/x$. If we let m vary from $-N$ to N, equation (13) is a linear system of equations for $g_n(\{r\}, \{x\})$ whose *Toeplitz* coefficient matrix is invertible because of the linear independence of the azimuthal functions $\{\exp(im\phi)|m \in [-N, N]\}$ over any finite interval $\phi \in [-\Phi, \Phi]$. This is an important result of the present paper.

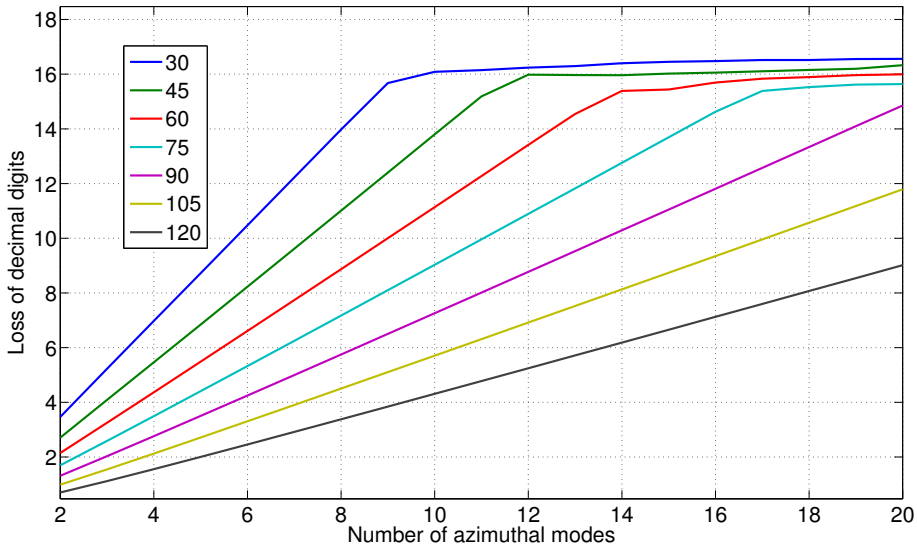

Figure 1. $\log_{10}$ **of condition number in matrix inversion for various sector sizes (degrees) and azimuthal mode numbers.**

While the coefficient matrix of equation (13) is nonsingular, its numerical *condition number*[a]

[a]Defined as the ratio of the largest singular value of the matrix to the smallest singular value

will deteriorate with decreasing sector size Φ and an increasing number of included azimuthal modes N. The base 10 logarithm of the condition number of a square matrix indicates the number of decimal digits of precision needed to invert this matrix. The usual 64 bit double precision IEEE floating point arithmetic used in contemporary computers provides approximately 16 decimal digits of precision, so when the base 10 logarithm of the condition number approaches 16, the matrix becomes too ill conditioned. In figure 1 we show the digit demand for a range of sector angles (in degrees) and highest azimuthal wave number. It can be seen that reasonable results are possible for a smaller number of azimuthal modes, say $N = 12$ and sector size, say $\Phi = 60°$.

Note that the main reason that we can recover the complete properties from observations on a sector is that the azimuthal modes have a priori *known global shapes* around the full circle; only the coefficients need to be estimated.

II.C. On the nature of azimuthal coherence

In this section we restrict the analysis to coherences between points on a ring corresponding to a constant radius and axial distance around an axisymmetric jet. Since the Fourier series of equation (10) must converge, for practical purposes we can choose a positive integer N, such that the crossspectral function for the ring may be written as

$$\Gamma(\phi_2, \phi_1) = \sum_{n=-N}^{N} g_n \exp\left(in(\phi_2 - \phi_1)\right). \tag{14}$$

The coherence is thus

$$\gamma^2(\phi_1, \phi_2) = \frac{\Gamma(\phi_1, \phi_2)\Gamma(\phi_2, \phi_1)}{\Gamma(0, 0)^2}, \tag{15}$$

and it can be seen from equations (14) and (15) that a necessary and sufficient condition for the coherence being unity is that there exists only one azimuthal wave number with nonzero amplitude.

II.D. Efficient spectral matrix estimation

Let us assume that we have made measurements with a microphone array that rotates with the azimuthal coordinate as defined in section II.B and denote the sets of sampled random vectors $\{p_k(\phi_1, \{r\}, \{x\})|k \in [1, K]\}$ and $\{p_k(\phi_2, \{r\}, \{x\})|k \in [1, K]\}$. The usual estimate for the crossspectral matrix function of equation (11) is then

$$G(\phi_1, \phi_2, \{r\}, \{x\}) = \frac{1}{K} \sum_{k=1}^{K} p_k(\phi_1, \{r\}, \{x\}) \overline{p_k(\phi_2, \{r\}, \{x\})}. \tag{16}$$

Since $G(\phi_1, \phi_2, \{r\}, \{x\})$ is a function of samples of the random vectors, in general

$$G(\phi_1, \phi_2, \{r\}, \{x\}) \neq G(\phi_1 + \phi_o, \phi_2 + \phi_o, \{r\}, \{x\}),$$

but it is trivially seen that

$$E(G(\phi_1, \phi_2, \{r\}, \{x\})) = \Gamma(\phi_2 - \phi_1, \{r\}, \{x\}). \tag{17}$$

We are thus led to an improved estimate of the crossspectral matrix function, which can be written as

$$\tilde{G}(\phi_1, \phi_2, \{r\}, \{x\}) = \frac{1}{2\pi} \int_{-\pi}^{\pi} G(\phi_1 + \phi_o, \phi_2 + \phi_o, \{r\}, \{x\}) d\phi_o, \tag{18}$$

whereby it is seen that

$$\tilde{G}(\phi_1, \phi_2, \{r\}, \{x\}) = \tilde{G}(0, \phi_2 - \phi_1, \{r\}, \{x\}) \text{ and } E(\tilde{G}(\phi_1, \phi_2, \{r\}, \{x\})) = \Gamma(\phi_2 - \phi_1, \{r\}, \{x\}). \tag{19}$$

This estimate will then have a smaller variance error than the raw estimate of equation (11) because of the averaging implicit in equation (18), and it will have the same location invariant matrix structure as the theoretical spectral matrix. Since the integration presumes a continuous scan in the azimuthal direction, we shall formulate a discrete data improved estimator in section (III.C).

III. Finite Analysis

III.A. Azimuthal coordinates in axisymmetric jets

We will limit our treatment to sound pressure measurements at a ring of microphones, uniformly spaced azimuthally such that the jet centerline is at the origin of the measurement ring, and that the ring is perpendicular to the jet axis. The assumptions of axisymmetry, including swirl then indicate that the spatial description of the sound fields would be simplified by using the complex exponentials around the circle as the natural azimuthal coordinates.

III.B. Pressure time history in azimuthal coordinates

Let us assume that we have N microphones, and consider the N by N matrix of complex exponentials

$$W = \frac{1}{\sqrt{N}} \begin{pmatrix} 1 & \dots & e^{2\pi i \frac{0m}{N}} & \dots \\ 1 & \dots & e^{2\pi i \frac{1m}{N}} & \dots \\ \dots & \dots & \dots & \dots \\ 1 & \dots & e^{2\pi i \frac{nm}{N}} & \dots \\ \dots & \dots & \dots & \dots \end{pmatrix}. \tag{20}$$

We see that column number m, starting from zero is a traveling wave with wave number m, matched by a complex conjugate column, indexed by $-m$ which represents a wave of the same wavenumber, but traveling in the opposite direction. We define the column number m as the vector W_m and note that $W_{N-m} = W_m$. We can easily see that the columns are mutually orthogonal, i.e., $W_n^H W_m = \delta_{nm}$. Also, we note that W is also the matrix form of the discrete Fourier transform of N points. Let us now denote the column vector time history of the microphone recordings as $P(t)$ and expand it in terms of the azimuthal modes W_m as

$$P(t) = \sum_{m=0}^{N-1} W_m \tilde{p}_m(t) = W \begin{Bmatrix} \tilde{p}_0(t) \\ \tilde{p}_1(t) \\ \vdots \\ \tilde{p}_m(t) \\ \vdots \end{Bmatrix} = W\tilde{p}(t). \tag{21}$$

Because of the orthogonality of the azimuthal modes, equation (21) gives us a very simple formula for calculating the azimuthal time histories

$$\tilde{p}(t) = W^H P(t). \tag{22}$$

We have shown earlier that for axisymmetric jets with axisymmetric boundary conditions and measurement locations, the composite sound field is a superposition of mutually incoherent pure

azimuthal modes, and hence that the expansion given in equation (21) has decoupled the measured vector time history into uncorrelated azimuthal time histories. We would then expect that the crossspectra in azimuthal coordinates would be zero, and that the autospectra would be close to the eigenvalues obtained by the conventional eigenvalue analysis of the autospectral matrix of the measured time histories as outlined below. The mutual incoherence between azimuthal modes, also between those with the same wave number but opposite polarity implies that even though the mean circumferential partial velocities are zero for jets without swirl, the standard deviation of the circumferential velocity can be large.

III.C. Improved axisymmetric estimator

Under the assumption of axisymmetry in the jet as well as in the instrumentation, the expected value of the autospectral matrix is invariant under cyclic permutations of the channel numbers, since we can start labeling the microphones from an arbitrary origin under the assumed instrumentation symmetry. The mathematical expression of a simple cyclic permutation of order N is the matrix

$$Q = \begin{pmatrix} 0 & 1 & 0 & 0 & \dots \\ 0 & 0 & 1 & 0 & \dots \\ 0 & 0 & 0 & 1 & \dots \\ \dots & \dots & \dots & \dots & \dots \\ 1 & 0 & 0 & 0 & \dots \end{pmatrix}, \tag{23}$$

whereby it can be seen that

$$Q^N = I \text{ and } Q \begin{Bmatrix} 1 \\ 2 \\ 3 \\ \vdots \\ N \end{Bmatrix} = \begin{Bmatrix} 2 \\ 3 \\ 4 \\ \vdots \\ 1 \end{Bmatrix}. \tag{24}$$

Now, let $\tilde{G}_{PP}$ be any *unbiased estimator*[b] of G_{PP}, i.e., $E(\tilde{G}_{PP}) = G_{PP}$. It then follows from the assumption of axisymmetry and equation (24) that for any integer k, $E(Q^k \tilde{G}_{PP} Q^{-k}) = G_{PP}$. Hence, the estimator

$$\bar{G}_{PP} = \frac{1}{N} \sum_{k=0}^{N-1} Q^k \tilde{G}_{PP} Q^{-k} \tag{25}$$

is unbiased, and its standard deviation is less than that of $\tilde{G}_{PP}$.

III.D. Partial field decomposition

When we are dealing with general geometries in jet nozzles and sensor placement, the usual way of decoupling the composite sound fields into coherent fields that combine in a sum squared fashion, is to perform an eigensolution of the autospectral matrix of the measurement channels. To each eigenvalue ρ_m^2, there corresponds an eigenvector V_m, normalized to unit magnitude, which we call a partial field, such that we may express the autospectral matrix as

$$G_{PP}(\omega) = \sum_{m=1}^{N} \rho_m^2(\omega) V_m(\omega) V_m^H(\omega). \tag{26}$$

[b]Note that an *estimator* is a random quantity, whereas the parameter to be estimated is deterministic.

When the underlying jet and instrumentation are axisymmetric, we expect the partial field decomposition to approximate the azimuthal coordinate decomposition, the advantage of the partial field decomposition being that it is purely data driven. We shall investigate whether the partial field and the azimuthal coordinate decomposition coincide for both axisymmetric model scale tests and LES computations, see sections V.B.1 and V.C.1. Note that we have included the generic frequency variable ω in this section, since we will be plotting the results of the analyses of the examples as a function of frequency.

IV. Sound flare model for turbulence mixing noise

The sound flare model was inspired by a recent paper by Papamoschou[10] where he constructed wave packets with desired azimuthal content by stochastically superposing the effects of regularly spaced localized azimuthal disturbances with a Gaussian shape. A *sound flare*[c] is the coherent sound field generated by a single random fluid dynamic event in a turbulent flow. The stationary incoherent superposition of an ensemble of such sound flares will then generate the total sound field. Such a description enables source models to describe auto- and crossspectra at any point on the measurement surface as well as locations radiating to the far-field. By definition, each coherent sound field results in a fixed phase relationship between any two points in space. These partial fields allow for partial coherence when superposed incoherently, as observed experimentally.

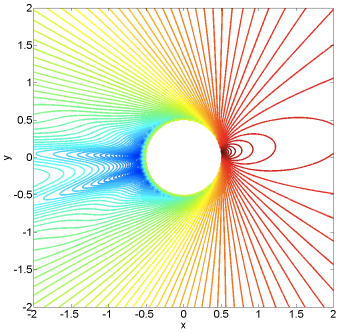

Figure 2. Pressure contour plot of 2D *sound flare* with strong directivity.

The motivation for the sound flare model was to show that a simple and plausible statistical model of fluid dynamic instabilities could generate the spectral function of the acoustic fields caused by turbulent mixing noise. It was also developed to be able to study the effects of axisymmetric as well as of general nozzles, and to understand the which of the transient instability properties are captured by the measured spectral function.

For simplicity in presenting the concepts, the paper will concentrate on the 2D sound flare model where the sound pressures are independent of the axial coordinate.

IV.A. The 2D sound flare model

We shall investigate sound flares in the azimuthal plane, invariant under translations in the axial coordinate x. This implies that disturbances in the out of plane direction conduct supersonically and have infinite wavelength. A single coherent field is generated by specifying a complex pressure distribution over the circumference of a circle with radius r_0, and extending this pressure distribution to the infinite cylinder along the jet axis. If we denote the pressure distribution on this surface as $p(\phi, r_0, x)$, its *helical spectrum* is given by the equation

$$\mathcal{P}_m(k_x) = \frac{1}{2\pi}\int_{-\pi}^{\pi} e^{-im\phi}\int_{\infty}^{\infty} e^{-ik_x x}p(\phi, r_0, x)dxd\phi, \tag{27}$$

and the induced pressure field exterior to the cylinder is given by the equation

$$p(\phi, r, x) = \frac{1}{2\pi}\sum_{m=-\infty}^{\infty} e^{im\phi}\int_{-\infty}^{\infty} e^{ixk_x}\mathcal{P}_m(k_x)\frac{H_m^{(1)}(k_r r)}{H_m^{(1)}(k_r r_0)}dk_x, \tag{28}$$

[c]We have chosen the term *sound flare* because of the similarity to *solar flares* which arise randomly, both spatially as well as temporally on the sun.

where $k_r = \sqrt{(k^2 - k_x^2)}$ and $H_m^{(1)}(k_r r)$ is the Hankel function of the first kind.[1]

Since the prescribed pressure on the cylinder is constant in the axial direction, equation (27) for the helical spectrum reduces to

$$\mathcal{P}_m = \frac{1}{2\pi} \int_{-\pi}^{\pi} e^{-im\phi} p(\phi, r_0, 0) d\phi, \tag{29}$$

and the induced pressure field in the azimuthal plane, equation (28), becomes

$$p(\phi, r) = \frac{1}{2\pi} \sum_{m=-\infty}^{\infty} e^{im\phi} \mathcal{P}_m \frac{H_m^{(1)}(kr)}{H_m^{(1)}(kr_0)} = \sum_{m=-\infty}^{\infty} e^{im\phi} \mathcal{A}_m(r). \tag{30}$$

Equation (30) states that the pressure distribution in the azimuthal plane is given as a sum of azimuthal modes, whose coefficients are given by

$$\mathcal{A}_m(r) = \frac{1}{2\pi} \frac{\mathcal{P}_m H_m^{(1)}(kr)}{H_m^{(1)}(kr_0)}. \tag{31}$$

We shown an example of a 2D sound flare in figure 3. The same sound field is shown as a contour plot in figure 2.

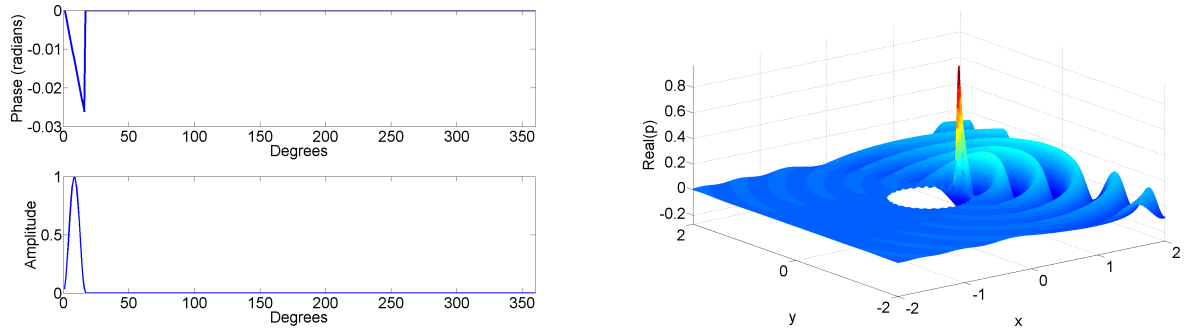

(a) Bode plot of complex pressure definition of sound flare. The swirl is indicated by the phase of the prescribed pressure field $p(\phi, r_0, 0)$.

(b) Real part of complex sound field generated by sound flare computed by equation (30).

Figure 3. Sound flare example with strong directivity and swirl

The generation of sound by stochastic processes (e.g., turbulence) is addressed next. The coherent sound field created by the prescribed pressure distribution is allowed to occur randomly at different azimuthal origins Φ governed by a probability distribution $h_A(\phi)$ such that the its cumulative distribution function is

$$pr(\Phi \leq \phi) = \int_0^{\phi} h_A(\alpha) d\alpha, \tag{32}$$

and the corresponding randomized sound pressure field is then

$$p(\phi - \Phi, r) = \sum_{m=-\infty}^{\infty} e^{2\pi i m(\phi - \Phi)} \mathcal{A}_m(r). \tag{33}$$

The cross-spectrum between any two points (α, r_1) and (β, r_2) is the integrated effect of all these localized *sound flares* over all possible values of ϕ, as given by equation (34). The measured coherence no longer has to be unity between the two points.

$$\Gamma(\{\alpha, r_1\}, \{\beta, r_2\}) = \int_0^{2\pi} h_A(\phi) p(\alpha - \phi, r_1) \overline{p(\beta - \phi, r_2)} d\phi. \tag{34}$$

IV.A.1. An axisymmetric nozzle

We now specialize to an axisymmetric jet. The sound flares are now equally likely in any azimuthal orientation, so the corresponding probability density function must be the uniform distribution,

$$h_A(\phi) = \frac{1}{2\pi}. \tag{35}$$

We insert equations (35) and (33) into equation (34), simplify and integrate to obtain

$$\begin{aligned}\Gamma(\{\alpha, r_1\}, \{\beta, r_2\}) &= \frac{1}{2\pi} \sum_{m=-\infty}^{\infty} \sum_{n=-\infty}^{\infty} \mathcal{A}_n(r_1)\overline{\mathcal{A}_m(r_2)} e^{i(n\alpha - m\beta)} \int_0^{2\pi} e^{i(n-m)\phi} d\phi \\ &= \sum_{n=-\infty}^{\infty} \mathcal{A}_n(r_1)\overline{\mathcal{A}_n(r_2)} e^{in(\alpha-\beta)}, \end{aligned} \tag{36}$$

since the integral is zero when $m \neq n$ because of the orthogonality of the complex exponentials over the unit circle. The expressions in equation (36) are found to be the summation of cross-spectra of each azimuthal mode, which proves that the azimuthal modes are pure and incoherent with one another. Thus for axisymmetric jets, partial fields and pure azimuthal modes are one and the same.

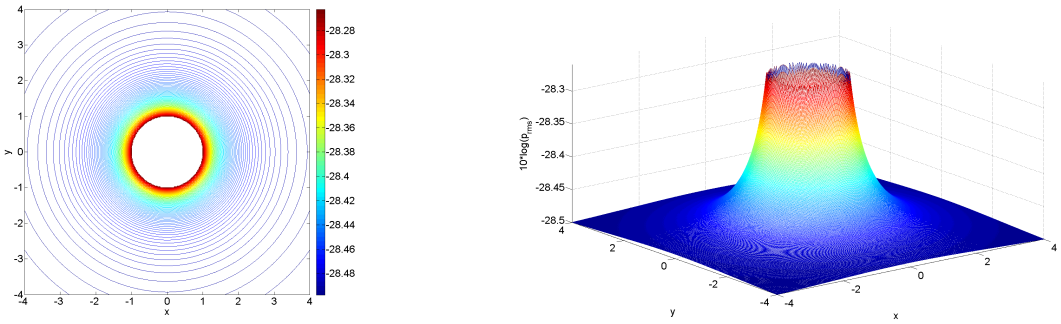

(a) Log magnitude contours of total sound pressure for uniform distribution of sound flare.

(b) Surface plot of log magnitude of total sound pressure, showing rapid nearfield decay (evanescence).

Figure 4. Resulting sum of squares total pressure for uniform sound flare distribution

In the original sound flare, equation (30), the azimuthal components summed up linearly, so one can now observe the effects of the phasing between the components. When looking at the complex sound field generated by randomizing around the 360°, the azimuthal components are now mutually incoherent and add up in a sum-of-squares fashion such that the phasing that defines the shape of the sound flare is lost, see equation (36). Each azimuthal component is now a partial field, and one can still recover the azimuthal component function up to an unknown phase angle. This proves that if partial fields are detected in a sector, they may also be described around the complete circle. This also says that several distinct flare patterns can generate identical complex sound fields; i.e., the coefficient of each azimuthal mode is the same as the coefficient in the sound flare.

Because the sound flares were randomized with uniform azimuthal distribution (i.e. they were axisymmetric), the plot of log magnitude of total sound pressure created by randomized sound flaresresults in an axisymmetric directivity pattern as shown in figures 4(a) and 4(b).

Figure 5(a) and figure 5(b) present the azimuthal coherence between two sensors with azimuthal spacing for the axisymmetric sound field. The plots are shown on a linear and a logarithmic ordinate, respectively, and demonstrate that there is partial and rapidly diminishing azimuthal coherence beyond a small angular spacing. Despite this short coherence length, the detected partial fields

have mode shapes that appear axisymmetric and global. For example, the real part of the leading three shapes is pictured in figure 5. The dominant mode in this example is clearly axisymmetric, while the second and third modes contain components of swirl in opposite directions. For this particular numerical example, the magnitudes of the singular values associated with each mode are plotted in figure 6 and indicate that beyond the axisymmetric mode that has the strongest magnitude, pairs of singular values associated with equal and opposite senses of rotation (i.e., positive and negative azimuthal modes) appear to characterize the sound field. This numerical model can thus be made to be entirely consistent with model scale and LES experiments performed at PSU that also give rise to such azimuthal mode pairing, as presented section V.B.1 and section V.C.1.

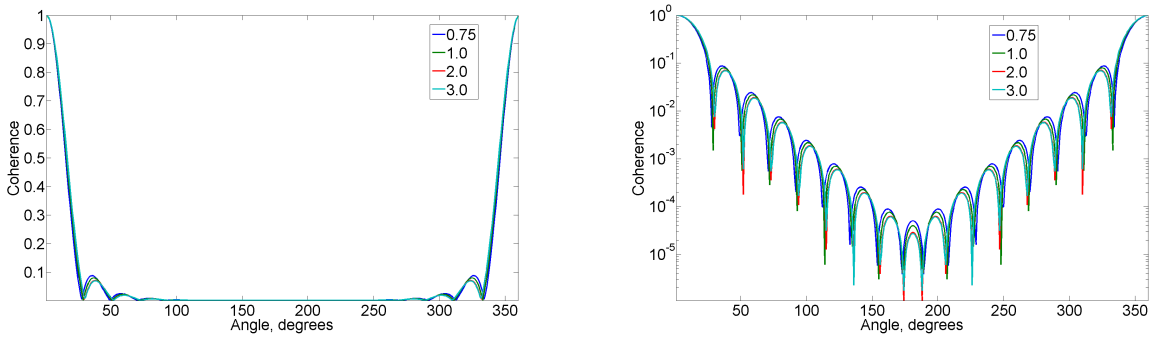

(a) Azimuthal coherence between any two sensors separated by angle , at four different radii.

(b) Same as figure on left, with log scale on ordinate.

Figure 5. Azimuthal coherences for uniform probability distribution

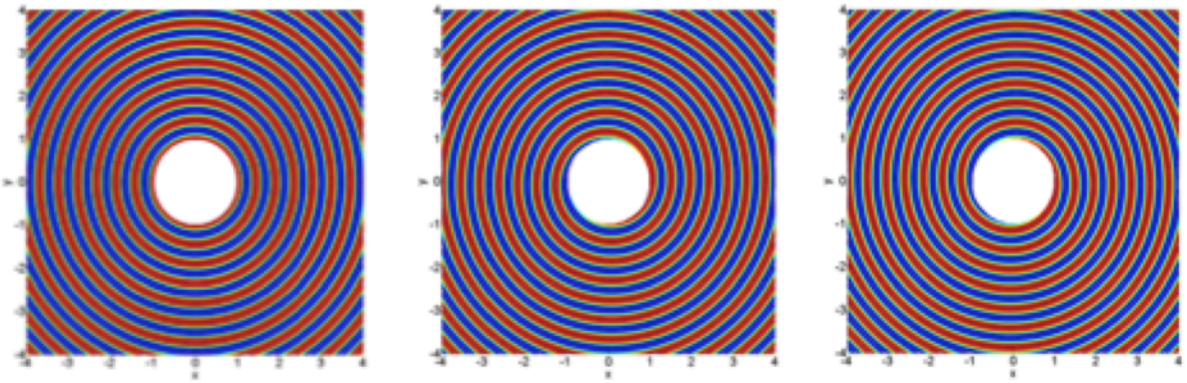

(a) Mode 1 (b) Mode 2 (c) Mode 3

Figure 6. Real part of detected partial field for the first three azimuthal modes that results from summing of sound flares.

In summary, in this section a numerical experiment was presented that demonstrates that the partial fields needed to describe the sound field can be described by global modes which can be detected by appropriately distributed sensors. Two important points are summarized below:

- One can stochastically sum sound flare or pure azimuthal modes; either way leads to the observations of same azimuthal coherences of short length.
- Even when the azimuthal coherence drops, the individual partial fields possess a fairly uniform amplitude as a function of azimuthal angle; hence, one can detect what is happening on the other side of the plume from measurements in a sector on one side of the plume.

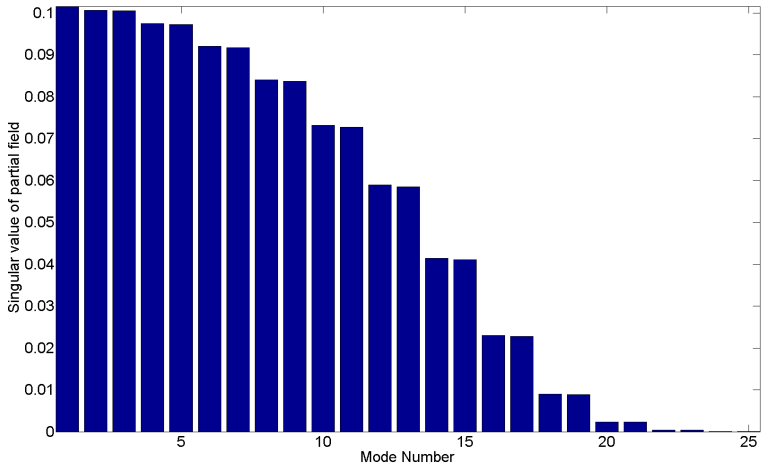

Figure 7. Magnitudes of singular values of composite sound field show leading singular value (from figure 6, associated with axisymmetric mode) followed by paired values associated with positive and negative higher aximuthal mode shapes.

- As long as only autospectra and crossspectra are being measured, it is not possible to ascertain the detailed shape of the sound flares that generated this field.

IV.A.2. A square nozzle

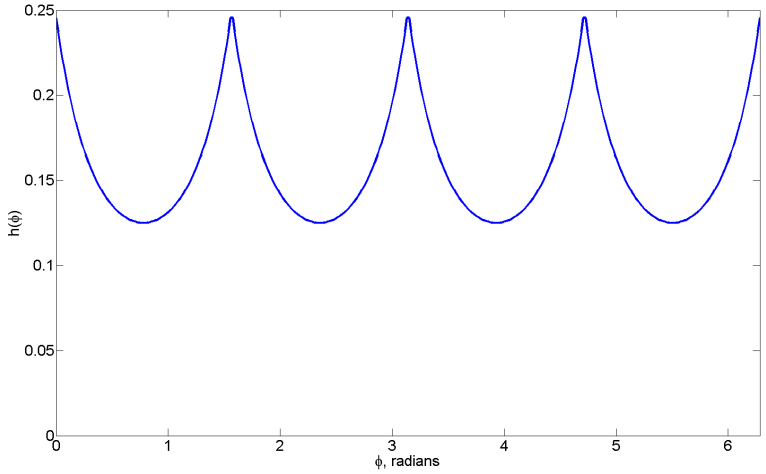

Figure 8. Probability distribution function for square nozzle $h_A(\phi)$.

This section presents a study of a simulated asymmetric nozzle. A diamond nozzle is considered, and a uniform probability density over the edges of a diamond surrounding the nozzle is used to simulated the statistics generated by sound flares (in this case, the same sound flare definition as used in the previous subsection which includes a component of swirl). When the probability density is plotted versus to the azimuthal angle as measured from the center of the jet, it generates the distribution shown in figure 8. A ring of sensors with an azimuthal spacing of one degree is simulated by constructing the spectral matrix and solving for eigenvalues and eigenvectors (partial

fields). Each partial field is then propagated from the pressures at the circle of 1 m radius to look at the near- and far-field behavior. Figure 9 presents a bar chart of the singular values or eigenvalues of the first twenty resultant fields, and figure 10 presents the real part of the primary partial fields for the leading nine modes. From the color contours, it is clear that these partial fields are also global modes, such that one may detect the whole field by observing a suitably large sector. Summing these eigenmodes by their respective weights results in the asymmetric sound field shown in figure 11(a) and figure 11(b), which is characteristic of the diamond nozzle. It is to be noted that the lack of mirror symmetry across the X and Y axes in the figure results from the small component of swirl associated with the original sound flare.

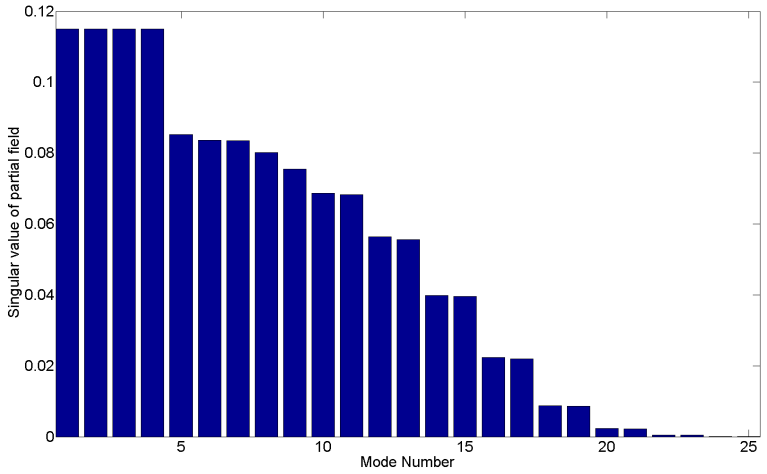

Figure 9. Magnitudes of singular values of composite sound field of *square nozzle* simulation.

IV.A.3. Detection of Asymmetric Partial Fields with Reference Sensors and Continuous Scanning

This section shows through numerical experiments that asymmetric partial fields with unusual directivity patterns can be reconstructed with an appropriate combination of reference and continuous-scan sensors.[12] An initial concept for sensor spacing is that it be fairly uniform according to the wavenumbers present, with enough irregularity to break any symmetries (to maximize the statistical information content).

The *virtual instrumentation* consists of a sector that is continuously scanned, giving a fine resolution of one degree, and a discrete set of reference sensors at the same radial distance but regularly spaced on the complement of the continuously scanned sector. In order to simulate a noise floor, random noise is added to the sound field 30 dB down from the highest amplitude recorded at $r = 1m$[d]. The coverage is judged on the fit of reconstruction to the underlying sound field. The following two points will be shown in this simplified 2-D example :

- A reasonably small continuously scanned sector will work from 50 Hz to 6000 Hz, with about 15 azimuthal reference microphones.
- Swirl and asymmetry present no problems.

For detection, an array radius of 3 m is selected over two sectors:

[d]This is just an arbitrary normalization since a noise floor is constant while the pressure fields decay away from the source

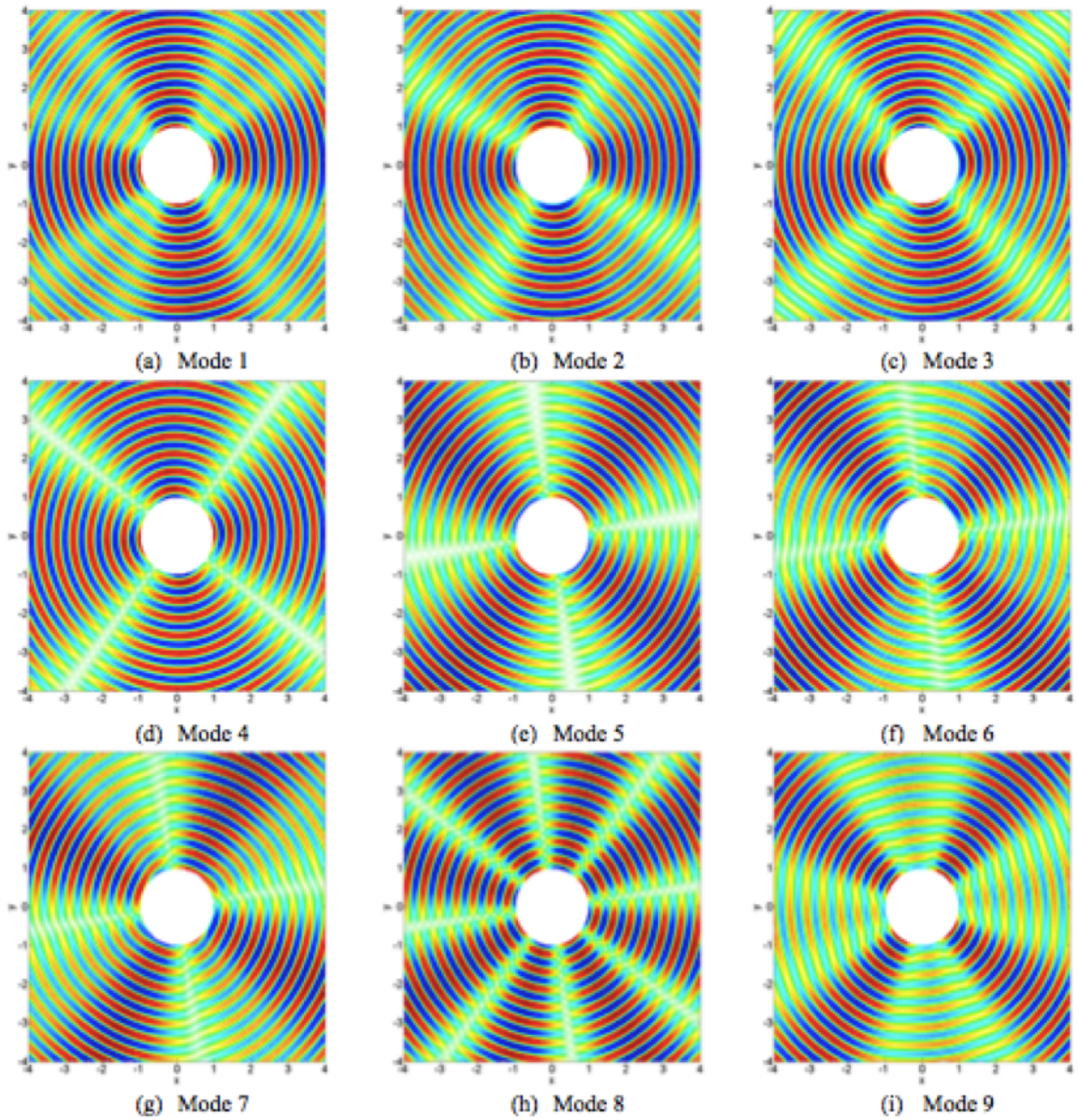

Figure 10. Real part of detected partial field for the first nine square nozzle modes that results from summing of sound flares.

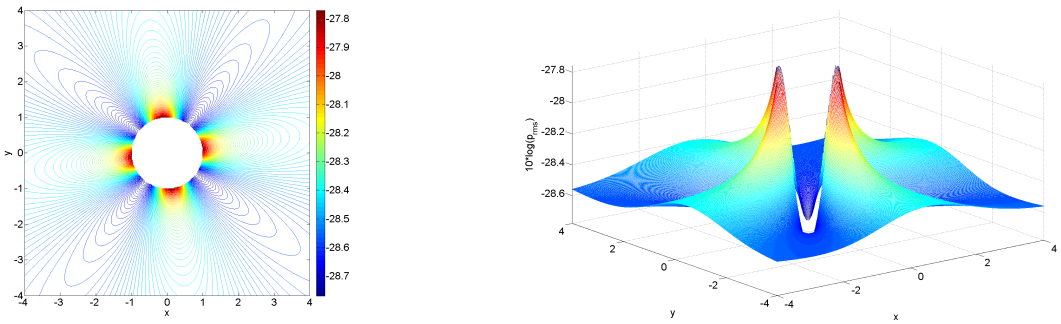

(a) Log magnitude contours of total sound pressure for square nozzle distribution of sound flare.

(b) Surface plot of log magnitude of total sound pressure, showing rapid nearfield decay (evanescence).

Figure 11. Resulting sum of squares total pressure for square nozzle sound flare distribution

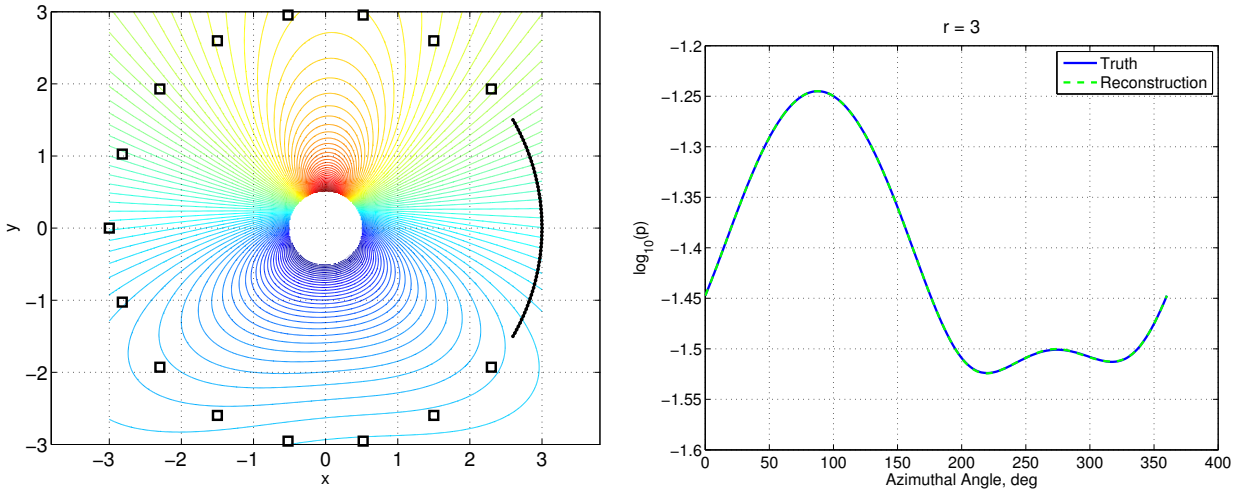

(a) Logarithmic sound pressure distribution contours. Squares indicate discrete microphone locations.

(b) Original (truth) and reconstruction at r=3 m.

Figure 12. Sound flare example at 50 Hz.

1. Continuous scan over [-30 30] degrees.

2. 15 evenly spaced reference microphones over [40 320] degrees.

The plots in figures 12 - 14 demonstrate that a 60° continuous-scan sector with 15 evenly spaced reference microphones are again able to reconstruct the underlying sound field to within the uncertainty of the noise floor[e] as can be seen in figure 14(b). Below the noise floor the reconstruction will be poor, but this is an inherent limitation of any such experiment. These numerical experiments ultimately suggest is that asymmetry and sound fields associated with swirl are in principle not a problem for the array in this example.

While the examples shown here are for 2-D sound fields, separation of variables will allow a straightforward extension of these approaches to 3-D sound fields provided that the reference sensors contain resolution in the axial and azimuthal degrees of freedom. Without loss of generality, the sensor arrangements shown in this section would also apply to irregularly spaced geometries and scanning surfaces that were not perfect surfaces of revolution. The key requirement is that the location of the proposed sensors is known to within a certain precision.

[e]The noise floor becomes visible in the reconstruction at frequencies higher than 1500 Hz

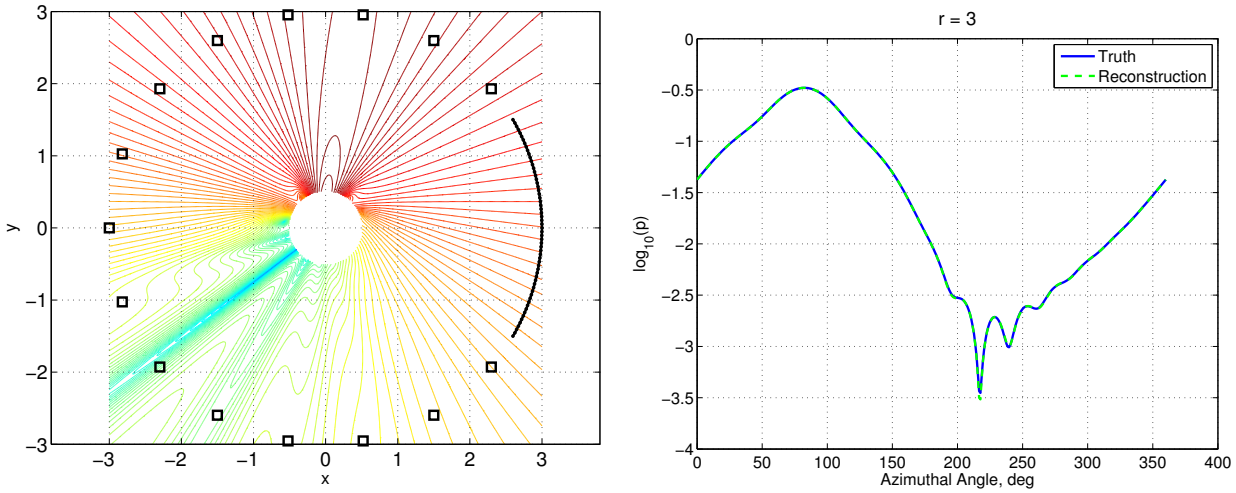

(a) Logarithmic sound pressure distribution contours.

(b) Original (truth) and reconstruction at r=3 m.

Figure 13. Sound flare example at 750 Hz.

IV.B. Foundations for a 3D sound flare model

We propose to use a formulation based on pressure source densities along the jet axis, rather than pressure distributions over cylinders.

A *3D sound flare* is pressure disturbance function $p(\phi, r, x)$ in cylindrical coordinates generated by a general line source which be written as

$$p(\phi, r, x) = \sum_{m=-\infty}^{\infty} e^{im\phi} \sum_{n \geq |m|}^{\infty} \int_0^L c_{mn}(l) P_n^m\left(\frac{x-l}{\sqrt{(x-l)^2 + r^2}}\right) h_n^{(1)}\left(k\sqrt{(x-l)^2 + r^2}\right) dl, \tag{37}$$

where k is the acoustic wavenumber, $P_n^m(\cos\theta)$ is the associated Legendre function[1] and $h_n^{(1)}(kr)$ is the spherical Hankel function of the first kind.[1]

Using equation (37) define the pressure field resulting from a point source at azimuthal angle α and axial position l as

$$p(\phi - \alpha, r, x, l) = \sum_{m=-\infty}^{\infty} e^{im(\phi-\alpha)} \sum_{n \geq |m|}^{\infty} c_{mn}(l) P_n^m\left(\frac{x-l}{\sqrt{(x-l)^2 + r^2}}\right) h_n^{(1)}\left(k\sqrt{(x-l)^2 + r^2}\right). \tag{38}$$

We want to view the parameters α and l as uncorrelated random variables, so we define the azimuthal probability density function as $h_A(\alpha)$ and the axial probability density function as $h_X(l)$. This allows us to define the crossspectrum between two points in 3D space analogously to equation (34) as

$$\Gamma(\{\alpha, r_1, x_1\}, \{\beta, r_2, x_2\}) = \int_0^{\infty} h_X(l) \int_0^{2\pi} h_A(\phi) p(\alpha - \phi, r_1, x_1, l) \overline{p(\beta - \phi, r_2, x_2, l)} d\phi dl. \tag{39}$$

A good choice for the axial probability density function could be the *lognormal* distribution since it will allocate most of the radiative energy close to the nozzle with a fast decay toward infinity.

The formulation in terms of spherical Hankel functions gives directly the proper farfield decay from a compact and finite sound source, $1/r$, and there are no end effects and aliasing due to the numerical Fourier transforms that are needed in the computations involving cylindrical Hankel functions, see equation (28).

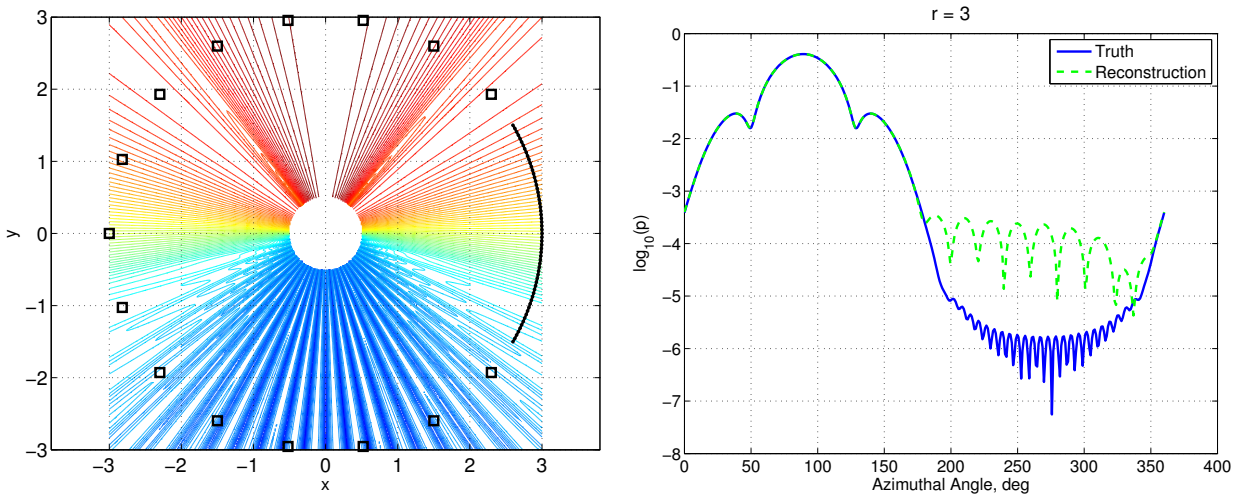

(a) Logarithmic sound pressure distribution contours.

(b) Original (truth) and reconstruction at r=3 m. Note noise floor at lower response levels.

Figure 14. Sound flare example at 6000 Hz.

V. Examples

In order to demonstrate the implementation of the analytical ideas in the previous sections they will be applied to both experimental measurements and data from numerical simulations.

V.A. A simple numerical example of spectral function recovery from partial azimuthal coverage

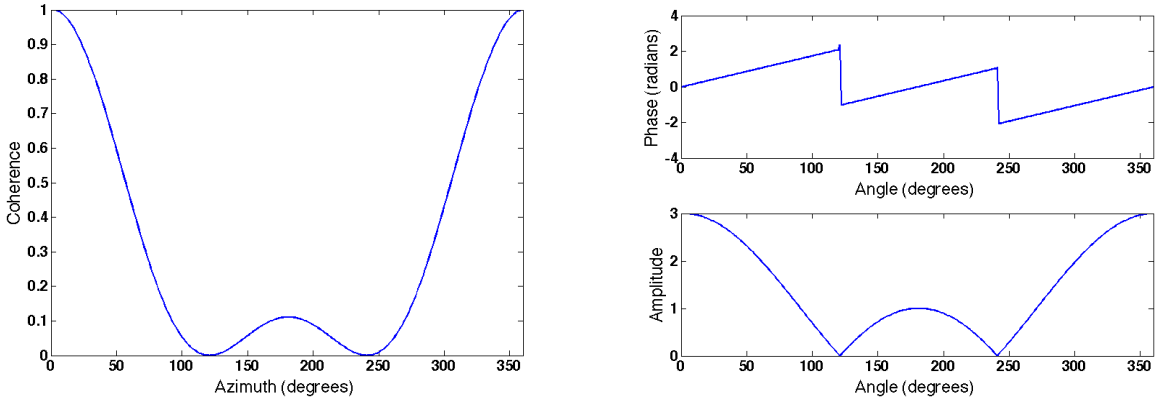

(a) Coherence.

(b) Crossspectrum phase and amplitude.

Figure 15. Numerical azimuthal example with $g_0 = g_1 = g_2 = 1$.

For this simple numerical example, we restrict the analysis to crossspectra between points on a ring corresponding to a constant radius and axial distance around an axisymmetric jet. Also, the sound field will be assumed to be composed of the first four azimuthal wavenumbers, such that the spectral matrix function may be specialized from equation (11) to the form

$$\Gamma(\phi_2 - \phi_1) = \sum_{n=-3}^{3} g_n \exp\left(in(\phi_2 - \phi_1)\right), \tag{40}$$

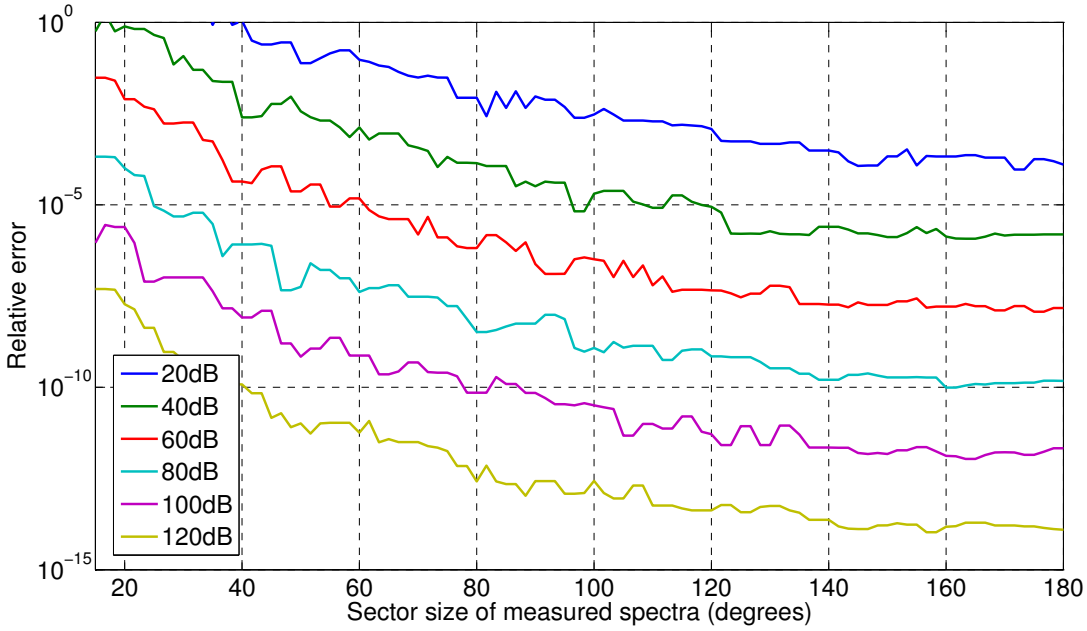

Figure 16. Relative error in estimating azimuthal modes, assuming 4 significant modes of both polarities, as functions of measured sector size. The S/N values are identified in the legend. Note that the relative error axis is clipped at one, since relative errors larger than one signify meaningless results

and furthermore we set all the g_n coefficients to zero except for g_0, g_1 and g_2, which receive unity values. The resulting coherence is shown in figure 15(a). Note that this sound field is the random superposition of three azimuthal fields with unit amplitude at any angle. This composite field also has swirl, since only the positive polarity azimuthal modes have nonzero magnitude; examine the phase of the crossspectrum on figure 15(b).

Now, we form the and solve equation (13) in 64 bit *IEEE* floating point arithmetic for azimuthal sector sizes $\Phi \in [15^\circ \ldots 180^\circ]$ with synthetic *signal to noise ratios* (S/N) from 20dB to 120dB. The relative error in the solution for the azimuthal modes are plotted on a logarithmic scale in figure 16. The relative error is defined as the norm of the true solution of equation (13) divided into the norm of the numerical minus the true solution.

V.B. A model scale axisymmetric supersonic jet

The experiments and simulations were conducted at Pennsylvania State University, see figure 17. A brief description of the experimental facility and measurements is given below.

The experiment was performed with axial positions of $x/D = 1$, 3 and 18. Only the $x/D = 3$ data are reported on here. The cold jets were run at Mach 1.5 and 1.7, with the latter data set showing a well defined screech. The data were acquired from a Mach 1.5 axisymmetric jet with an exit diameter of 0.5 inches and a microphone ring radius of 2.5 inches as shown in figure 17(a). The experiments presented in this paper were conducted in The Pennsylvania State University high-speed jet noise facility shown in figure 17(b). The jet noise anechoic chamber facility is a 5.02 x 6.04 x 2.79 m. room covered with fiberglass wedges and with an approximate cut-on frequency of 250 Hz.

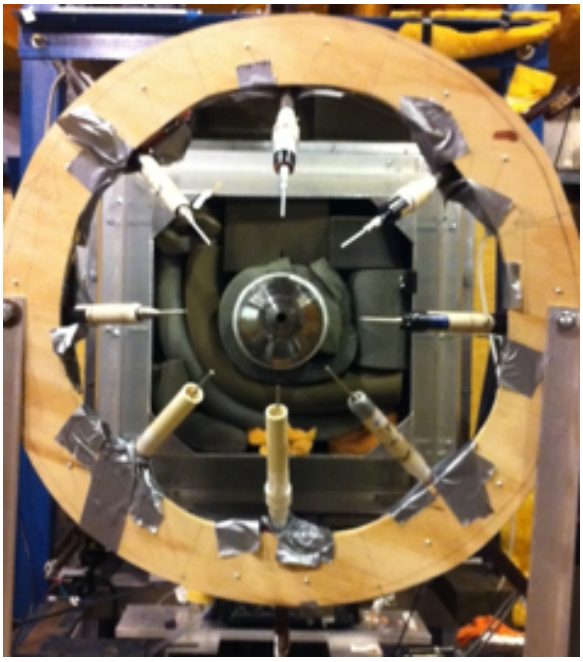

(a) Microphone ring and nozzle

(b) Test fixture setup

Figure 17. Penn State model scale test.

V.B.1. The experimental model scale data at Mach 1.5

The spectral data for the model scale test was processed with both the general partial field eigenanalysis, as well as being expressed in analytic azimuthal coordinates. The improved spectral matrix estimator described in section III.C was used. Figure 18 shows the plot of the amplitudes of the partial fields as a function of frequency in 18(a), and the autospectra of the azimuthal components in 18(b). The two sets of results are virtually identical when subjected to a visual comparison. We see clearly the presence of pairs azimuthal modes with opposite polarity, as well as the isolated axisymmetric mode.

V.B.2. Experimental model scale overexpanded jet with screech at Mach 1.7, partial fields and azimuthal modes

Next we look at the model scale cold jet running at Mach 1.7 in an overexpanded condition which results in screech tones. This can be seen in figure 19 where the azimuthal autospectra are plotted. Just as in the Mach 1.5 case (figure 18), the geometry incognizant partial field decomposition is virtually the same as the azimuthal coordinate decomposition, so we proceed to zoom into the frequency range of the first screech to compare the azimuthal coordinates with the partial fields.

The partial field plot around the screech, figure 20, shows that the amplitudes of the individual fields do not cross. The eigensolution process extracts for each frequency the partial fields of the largest amplitudes first. Next inspect the plot of the azimuthal coordinates, figure 21. We see that as we approach the screech frequency from the lower frequencies that azimuthal modes ± 1 start dominating the axisymmetric mode and as we get closer, the azimuthal mode -1 becomes dominant. This means that the pressure field is dominated by ovaling, and as we encounter the screech frequency the ovaling precesses in the counterclockwise direction. Once past the screech

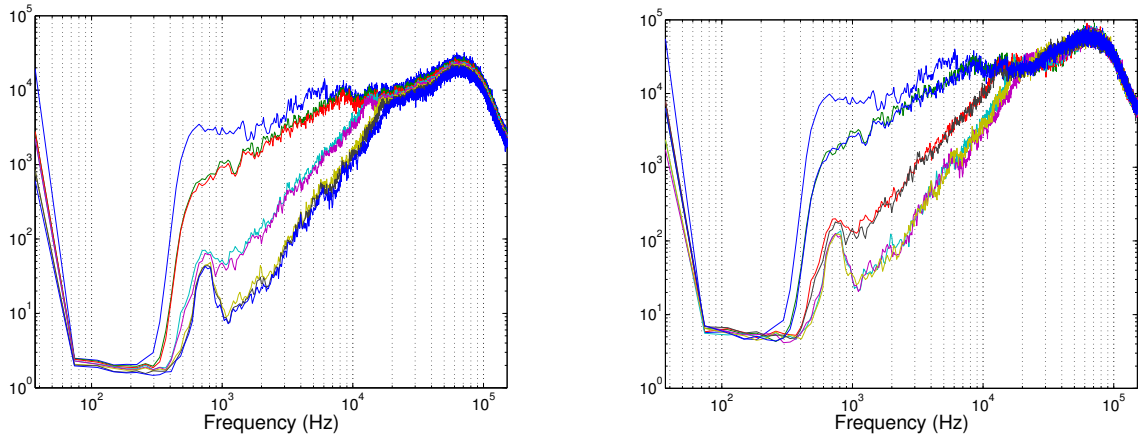

(a) Partial fields of the full autospectral matrix

(b) Autospectra of all eight azimuthal coordinates

Figure 18. Lab test data : partial field amplitudes and the autospectra of the channels in azimuthal coordinates; The partial fields do not consider geometry, whereas the azimuthal modal coordinates do.

frequency, the +1 mode dominates, such that the precession has changed polarity. This shows that swirl is possible also in an axisymmetric jet. For an extensive discussion of the physics of screech, see e.g., Raman.[18]

V.B.3. Experimental model scale overexpanded jet with screech at Mach 1.7, partial azimuthal coverage results

We now proceed to investigate the capabilites of a partial azimuthal coverage and restrict the data set to five adjacent microphones, such that we only have measurements in an 180° sector. We use the techniques from section II.B to recover the full spectral matrix, extract the partial fields, and plot their magnitude as a function of frequency in figure 22. When compared with the azimuthal coordinate plot from the 360° coverage in figure 19 we note that the global features match very well, but there seems to be fewer than 8 distinct function traces in the partial fields from the reduced coverage computations. We have ascertained that there is a rank loss in the matrix computations since there are only five data streams and we want to estimate the eight dominant partial fields. The function traces for the pairs of ± polarity modes tend to coincide, so we lose the indication of precessing swirl at the screech frequency range. Otherwise the results are reasonable. From a mathematical point of view, this problem could have been avoided if we had had at least 8 microphone channels in the 180° sector, but we lack the experimental data to corroborate this claim at the present time.

V.B.4. Experimental model scale overexpanded jet with screech at Mach 1.7, incoherence of individual azimuthal modes

We also show that the modes of the same wavenumber but opposite polarity are mutually incoherent by calculating their cross spectrum and autospectra and from that the ordinary coherence, shown in the two plots in figure 23. This further confirms the theoretical results from section II.A.2 that the azimuthal modes are mutually incoherent. A notable rise in coherence occurs at the two screech frequencies. This paper offers no explanation, even though it most likely involves known phenomena.[18]

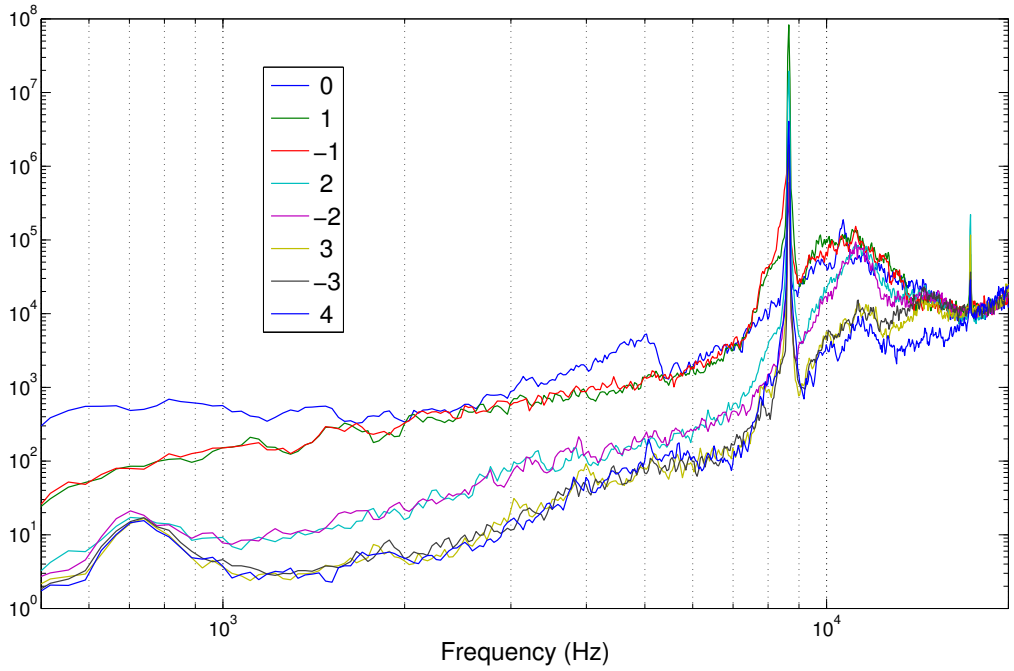

Figure 19. Autospectra of Mach 1.7 screeching jet at axial distance $x/D = 3$ in azimuthal coordinates. Note screech tone around 8.7 KHz.

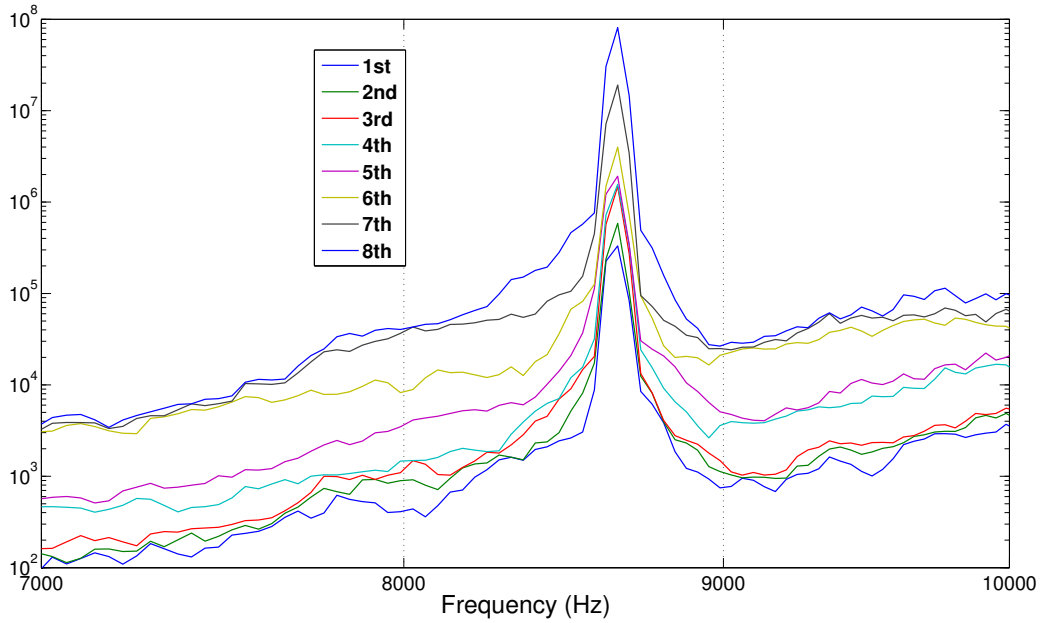

Figure 20. Mach 1.7 with screech zoomed : partial field amplitudes. The partial fields are organized by amplitude only since geometry information is not utilized. Inspection of the partial field shapes is needed to identify which azimuthal modes they represent.

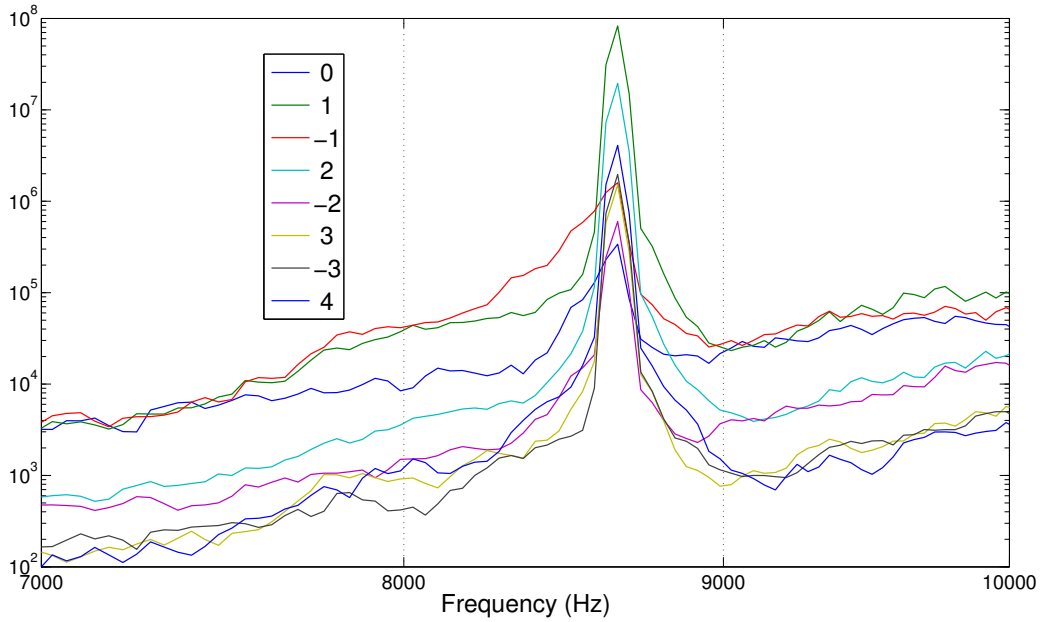

Figure 21. Mach 1.7 with screech zoomed : autospectra in azimuthal coordinates. Notice swirl precessing and changing polarity as we cross the screech frequency.

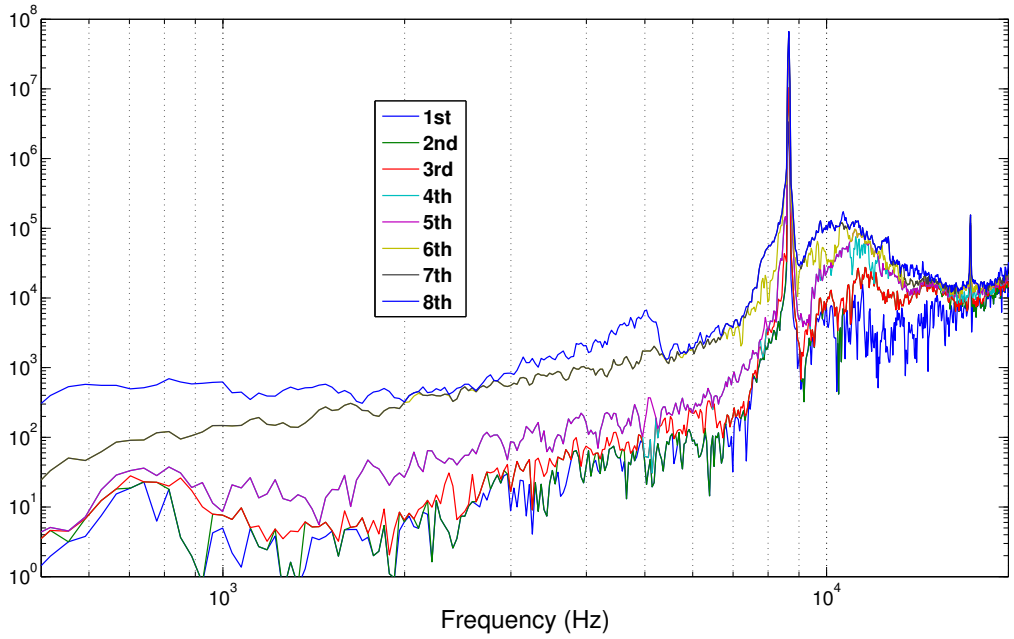

Figure 22. Mach 1.7 with screech : partial field amplitudes from 180° coverage, 5 microphones.

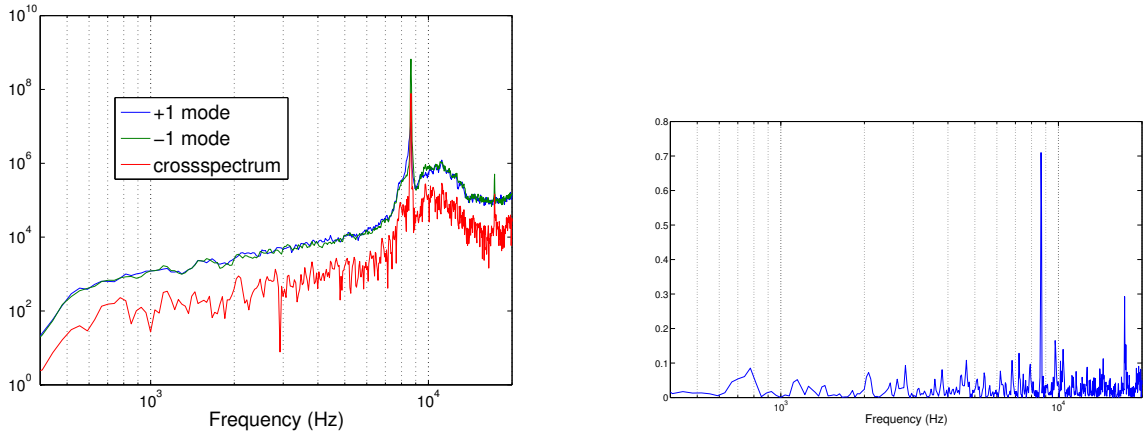

(a) Autospectra and crossspectrum for azimuthal modes ±1

(b) Coherence between azimuthal modes +1 and -1

Figure 23. Mach 1.7 with screech : The crosspectrum between azimuthal modes ±1 is drastically down from the autospectra. The coherence between the two is close to zero except for a coherence peak at the screech frequency where the two modes change dominant roles in the precession of swirl.

V.B.5. Experimental model scale overexpanded jet with screech at Mach 1.7, insufficiency of the discrete cosine transform *formulation in describing azimuthal coordinates*

In a paper by Fuchs and Michalke,[19] there is a description a procedure based on the *discrete cosine transform* to extract the azimuthal modes from measured data. Their derivation explicitly dismiss swirl as a phenomenon unlikely to be observed in axisymmetric jets unless it is superposed on the jet at the nozzle. Under this assumption, the opposite polarity mode pairs will have the same amplitude, and no mean circumferential bias would be expected. They proceed to develop this procedure, whereby just the amplitude of the mode pairs is estimated.

The present experiment represents a data set with swirl happening around a screech condition, section V.B.2, where this procedure will fail. Also, since we have shown that two modes of opposite polarity are stochastically independent, section V.B.4, the standard deviation of circumferential particle velocity will be non zero even when the mode pairs have identical amplitudes. We conclude that the discrete cosine transform procedure is deficient in characterizing the azimuthal modes of an axisymmetric jet lacking bilateral symmetry of its mean fluid motion.

V.C. LES experiment

A series of LES simulations of a supersonic fully expanded jet at 1.5 Mach have been conducted, a cut-plane image of which is shown in figure 24. The details of the numerical approach have been described by Morris and Du[20,21] The approach uses a multiblock structured mesh with both matching and non-matching interfaces. Spatial discretization is performed with a 7 point stencil, fourth-order accurate DRP scheme. Dual timestepping is used with both multigrid and implicit residual smoothing to accelerate the convergence of the sub-iterations. The radiated noise is predicted using solutions to the Ffowcs Williams and Hawkings equation[22] and a permeable acoustic data surface. The data used for the present analyses were taken from saved time histories at the acoustic data surface, with *virtual microphones* placed with an azimuthal spacing of 3° at various axial and radial locations.

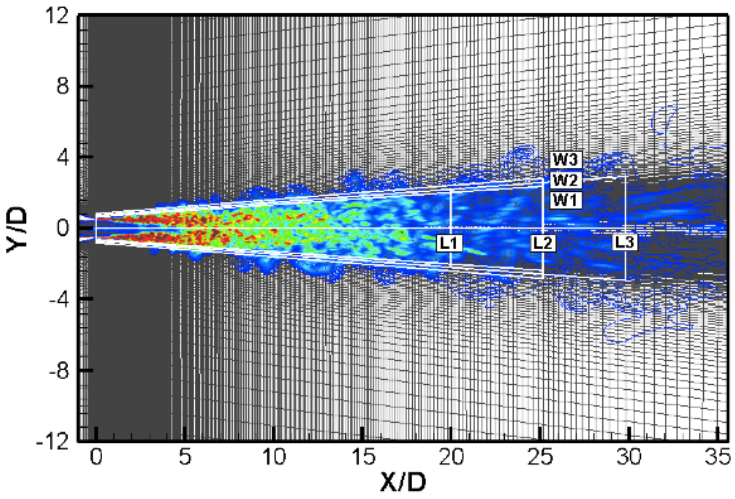

Figure 24. Instantaneous LES visualization of contours of X// of plume on a cutting plane through the jet centerline.

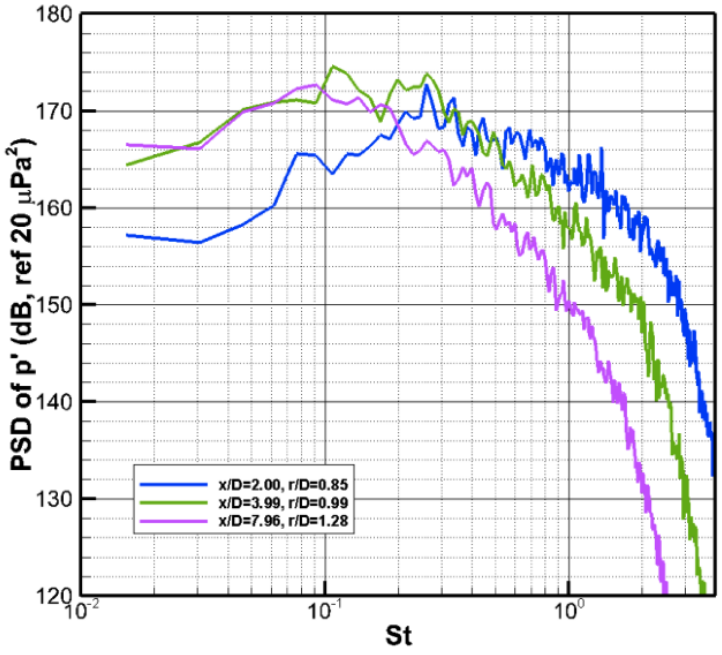

Figure 25. Sample pressure spectra close to the shear layer.

V.C.1. Comparison of azimuthal modes and partial fields for LES data

The same two procedures were repeated for the LES data, and the results are presented in figure 26. Here visual inspection shows a trifle more differences than in the lab test data, but much of this may be blamed on the much shorter length of the data set for the LES experiment, leading to higher statistical variability. Here we also see a trend for the data to organize itself into modal pairs with opposite polarity.

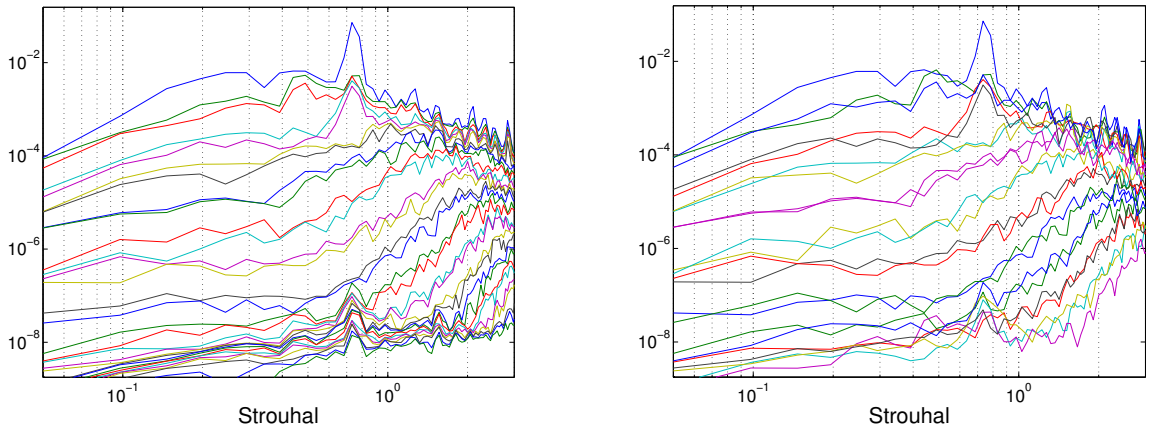

(a) Partial fields of full autospectral matrix (b) Autospectra of dominant azimuthal coordinates

Figure 26. LES data : partial field amplitudes and the autospectra of the channels in azimuthal coordinates.

V.C.2. Azimuthal Coherence from LES Data

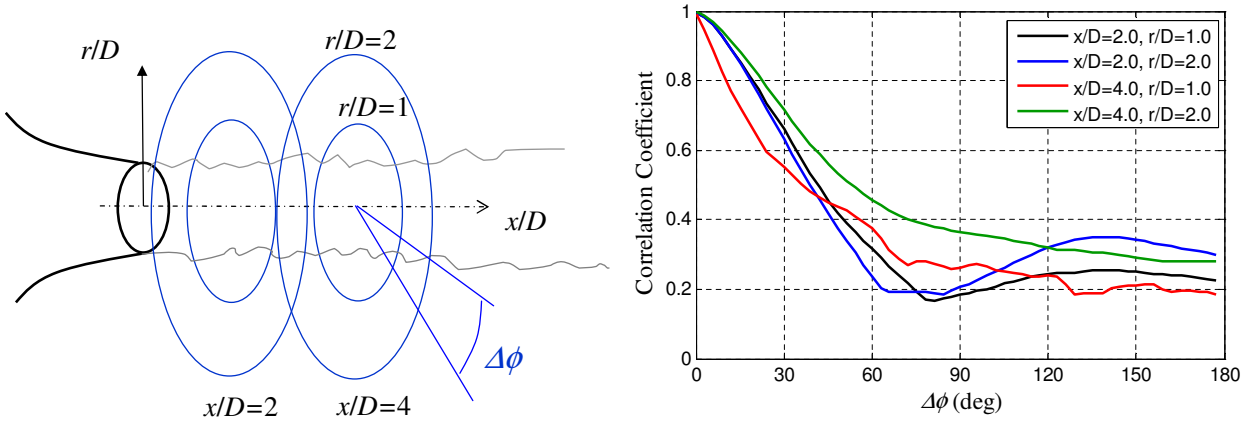

(a) Probe locations in LES domain. (b) Azimuthal pressure correlations from LES data.

Figure 27. LES azimuthal coherence processing.

The azimuthal coherence of the near-pressure field is a central quantity of interest in the present study. Experimental measurements of near-field azimuthal coherence at fine resolution are rare, a notable exception being that of Ukeiley and Ponton.[23] Probe interference is an obvious obstacle for such measurements, especially at very small scales. The advent of *Large Eddy Simulation* (LES) offers an unprecedented opportunity to evaluate correlations at arbitrary locations in the flow field, including two-point, space-time correlations that are critical for modeling jet noise. Here we use recent LES data generated at Penn State University for a supersonic jet with Mach number

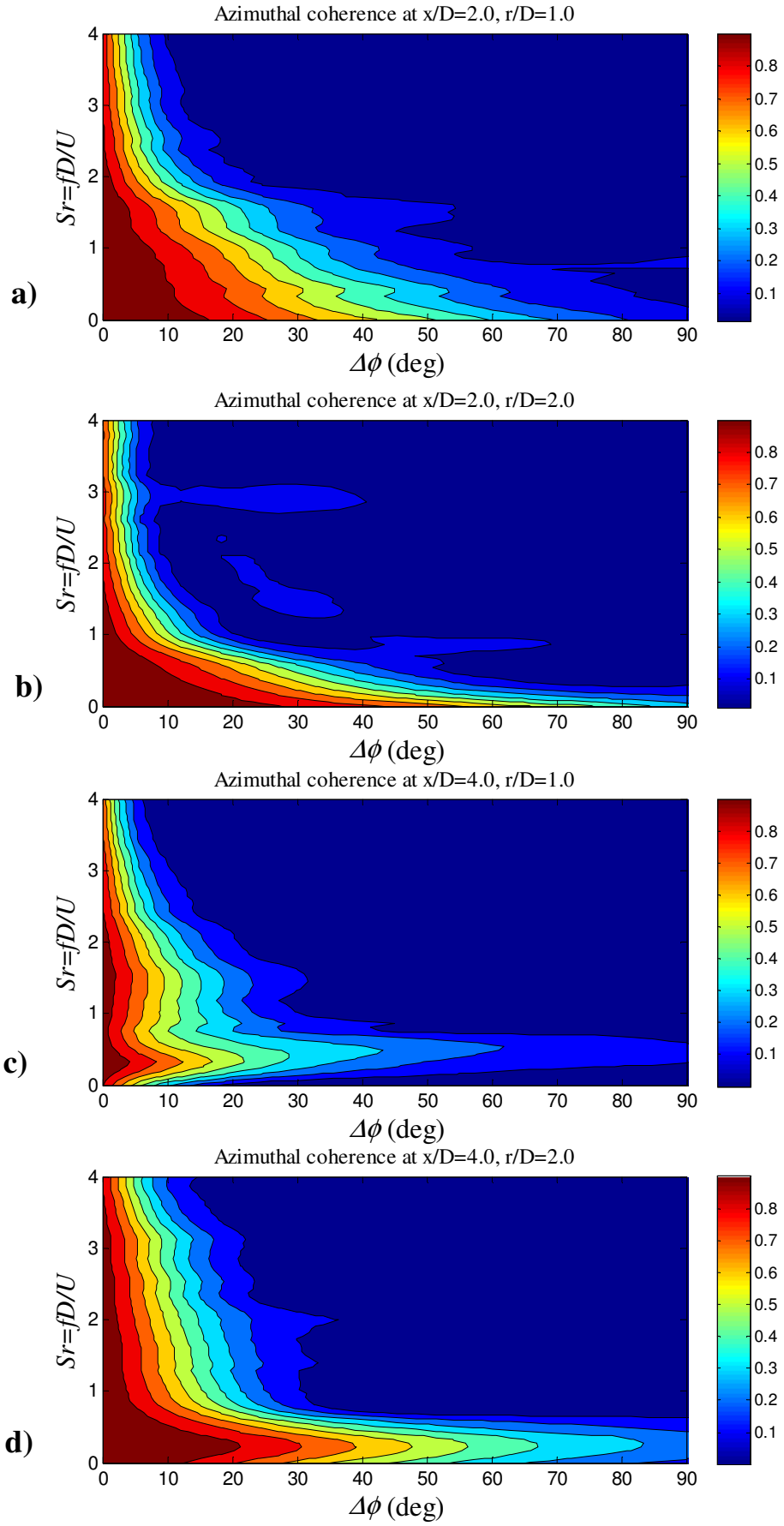

Figure 28. Azimuthal coherence from LES data. a) $x/D = 2, r/D = 1$; **b)** $x/D = 2, r/D = 2$; **c)** $x/D = 4, r/D = 1$; **d)** $x/D = 4, r/D = 2$.

$M = 1.47$ and velocity $U = 417$ m/s. We compute azimuthal correlations at axial locations $x/D = 2$ and 4, and radial distances $r/D = 1$ and 2. The measurement locations are shown in figure 27(a).

First we examine the correlation coefficient versus azimuthal spacing $\Delta\phi$. The plots of figure 27(b) show a rapid decline of the correlation with increasing azimuthal separation, followed by a plateau at low correlation value. The uplift of the curves at $x/D = 2$ are a numerical consequence of short record lengths inherent in the LES computation. Nevertheless, there is a remarkable similarity between the LES correlations of figure 27(b) and the experimental azimuthal correlations in a transonic jet by Ukeiley and Ponton,[23] at the same measurement locations. See also the paper by Tinney and Jordan.[24] With increasing x/D, the correlation curves becomes fuller (decline is less steep) due to stronger low-frequency content coming from the large-scale turbulent structures.

Next we examine the coherence γ^2 (equation 15) versus azimuthal separation. The coherence was computed using the MSCOHERE function of Matlab with FFT size of 512. The coherence results are presented as contour plots of γ^2 versus Strouhal number$Sr = fD/U$ and azimuthal separation $\Delta\phi$. To aid in the presentation of the plots, the coherence was smoothed moderately versus frequency using a Savitzky-Golay filter. It was ensured that the filtering did not alter the fundamental shape of the plot. Figure 28 presents the contour plots of azimuthal coherence for all the measurement locations. At the upstream locations, $x/D = 2$, the coherence decays monotonically with Strouhal number. Increasing the radial distance results in stronger coherence at low Strouhal number, a trend that may be related to the spreading of a localized azimuthal disturbance.[10] For the downstream stations, $x/D = 4$, the coherence displays a maximum near $Sr = 0.2$, the Strouhal number of peak noise emission from large-scale structures. Increase in radial location again strengthens the coherence at low frequency. What is notable in all the results is how weak the azimuthal coherence is at moderate and high frequencies. For example, at $Sr = 2$, the coherence drops to 0.5 for $\Delta\phi \approx 5^\circ$ at $x/D = 2$, and $\Delta\phi \approx 10^\circ$ at $x/D = 4$. Similar trends of sharply declining coherence with frequency are seen in the axial correlations of Tinney and Jordan[24] in the near field of a coaxial jet.

VI. Conclusions

In this paper we have shown how the axisymmetry of a jet engine induces properties that have important benefits for noise measurement procedures.

1. We have a complete decoupling of azimuthal and axial components in the POD modes of the noise field.

2. The complete matrix of autospectra and cross-spectra may be reconstructed from acoustic measurements in a regular over a reasonably small sector, less than 180 degrees.

3. The total acoustic field may be reconstructed by a sum of mutually incoherent azimuthal wave packets, where the spectral measurements have been taken on an irregular grid in a reasonably small azimuthal sector.

4. Since a smaller measurement sector suffices for determination of spectral quantities and parametric noise field modeling, we have the option of either reducing instrumentation budgets, or measure at a higher spatial resolution, which allows the analysis of higher frequency and wavenumber ranges.

5. The sound flare modeling shows that many features in the individual pressure disturbance events are not reflected in the measured crossspectral function, i.e., *second order statistics* give a globalized, ensemble view of the stationary pressure fields, such that higher order statistics are needed to capture the transient nature of the origins of the jet noise.

6. The fixturing of instrumentation for the measurement of full scale jets becomes simplified, since we may avoid having to straddle a nasty meandering plume.

Acknowledgements

The authors would like to thank Dr. Dennis McLaughlin of Penn State University and his students for organizing and executing the model scale experiments that provided the data for the axisymmetric supersonic jet used in the numerical examples section of this paper (section V.B).

Thanks are also extended to US Navy through NAVAIR for their support under Phase I SBIR Contract No. N68335-11-C-0466, with Dr. John Spyropoulos as technical monitor who especially suggested that we also investigate asymmetric nozzles.

References

[1]Abramowitz, M. and Stegun, I., *Handbook of mathematical functions with formulas, graphs, and mathematical tables*, Vol. 55, Dover publications, 1964.

[2]Morris, P., "The instability of high speed jets," *International Journal of Aeroacoustics*, Vol. 9, No. 1, 2010, pp. 1–50.

[3]Morris, P., "Viscous stability of compressible axisymmetric jets," *AIAA Journal*, Vol. 21, 1983, pp. 481.

[4]Morris, P. and Tam, C., "On the radiation of sound by the instability waves of a compressible axisymmetric jet," *Mechanics of sound generation in flows*, Vol. 1, 1979, pp. 55–61.

[5]Tam, C. and Burton, D., "Sound generated by instability waves of supersonic flows. Part 2. Axisymmetric jets," *Journal of Fluid Mechanics*, Vol. 138, No. 1, 1984, pp. 273–295.

[6]Tam, C., "Supersonic jet noise," *Annual Review of Fluid Mechanics*, Vol. 27, No. 1, 1995, pp. 17–43.

[7]Crighton, D. and Huerre, P., "Shear-layer pressure fluctuations and superdirective acoustic sources," *Journal of Fluid Mechanics*, Vol. 220, No. 1, 1990, pp. 355–368.

[8]Avital, E., Sandham, N., and Luo, K., "Mach wave radiation by mixing layers. Part I: analysis of the sound field," *Theoretical and computational fluid dynamics*, Vol. 12, No. 2, 1998, pp. 73–90.

[9]Morris, P., "A note on noise generation by large scale turbulent structures in subsonic and supersonic jets," *International Journal of Aeroacoustics*, Vol. 8, No. 4, 2009, pp. 301–315.

[10]Papamoschou, D., "Wavepacket Modeling of the Jet Noise Source," AIAA 2011-2835, June 2011.

[11]Papamoschou, D., "Prediction of Jet Noise Shielding," *Proceedings of the 48th AIAA Aerospace Sciences Meeting, AIAA Paper*, Vol. 653, 2010, p. 2010.

[12]Vold, H., Shah, P., Davis, J., Bremner, P., McLaughlin, D., Morris, P., Veltin, J., and McKinley, R., "High-Resolution Continuous Scan Acoustical Holography Applied to High-Speed Jet Noise," AIAA 2010-3754, June 2010.

[13]Vold, H., Shah, P., and Yang, M., "On the computation of farfield cross-spectra and coherences from reduced parameter models of high speed jet noise." *The Journal of the Acoustical Society of America*, Vol. 130, No. 4, 2011, pp. 2512.

[14]Shah, P., Vold, H., and Yang, M., "Reconstruction of Far-Field Noise Using Multireference Acoustical Holography Measurements of High-Speed Jets," AIAA 2011-2772, June 2011.

[15]Suzuki, T. and Colonius, T., "Instability waves in a subsonic round jet detected using a near-field phased microphone array," *Journal of Fluid Mechanics*, Vol. 565, No. 1, 2006, pp. 197–226.

[16]Reba, R., Simonich, J., and Schlinker, R., "Sound radiated by large-scale wave-packets in subsonic and supersonic jets," 2009.

[17]Schlinker, R., Reba, R., Simonich, J., Colonius, T., Gudmundsson, K., and Ladeinde, F., "Towards prediction and control of large-scale turbulent structure supersonic jet noise," *Proceedings of ASME Turbo Expo*, 2009.

[18]Raman, G., "Advances in understanding supersonic jet screech: review and perspective," *Progress in aerospace sciences*, Vol. 34, No. 1-2, 1998, pp. 45–106.

[19]Fuchs, H. and Michalke, A., "On turbulence and noise of an axisymmetric shear flow," *J. Fluid Mech*, Vol. 70, No. 1, 1975.

[20]Morris, P., Du, Y., and Kara, K., "Jet noise simulations for realistic jet nozzle geometries," *Procedia Engineering*, Vol. 6, 2010, pp. 28–37.

[21]Du, Y., *Supersonic jet noise prediction and noise source investigation for realistic baseline and chevron nozzles based on hybrid RANS/LES simulations*, Ph.D. thesis, The Pennsylvania State University, 2012.

[22]Ffowcs Williams, J. and Hawkings, D., "Sound generation by turbulence and surfaces in arbitrary motion," *Philosophical Transactions of the Royal Society of London. Series A, Mathematical and Physical Sciences*, Vol. 264, No. 1151, 1969, pp. 321–342.

[23]Ukeiley, L. and Ponton, M., "On the Near Field Pressure of a Transonic Axisymmetric Jet," *AIAA Journal*, Vol. 40, 2002, pp. 1735–1744.

[24]Tinney, C. and Jordan, P., "The near pressure field of co-axial subsonic jets," *Journal of Fluid Mechanics*, Vol. 611, 2008, pp. 175–204.